micromachines

MDPI

Review

2D MXene Nanomaterials as Electrocatalysts for Hydrogen Evolution Reaction (HER): A Review

Shaik Gouse Peera [1,*,†], Ravindranadh Koutavarapu [2,†], Liu Chao [3], Lakhveer Singh [4,5], Govindhasamy Murugadoss [6] and Gaddam Rajeshkhanna [7,*]

1 Department of Environmental Science, Keimyung University, Dalseo-gu, Daegu 42601, Korea
2 Department of Robotics Engineering, College of Mechanical and IT Engineering, Yeungnam University, Gyeongsan 38541, Korea
3 Engineering Research Center for Hydrogen Energy Materials and Devices, Faculty of Materials Metallurgy and Chemistry, Jiangxi University of Science and Technology, Ganzhou 341000, China
4 Department of Chemistry, Sardar Patel University, Mandi 175001, Himachal Pradesh, India
5 Department of Civil Engineering, Center for Research & Development, Chandigarh University, Mohali 140413, Punjab, India
6 Centre for Nanoscience and Nanotechnology, Sathyabama Institute of Science and Technology, Chennai 600119, Tamilnadu, India
7 Department of Chemistry, National Institute of Technology Warangal, Warangal 506004, Telangana, India
* Correspondence: gouse@kmu.ac.kr (S.G.P.); grkhanna@nitw.ac.in (G.R.)
† These authors contributed equally to this work.

Abstract: MXenes, a novel family of 2D transition metal carbide, nitride and carbonitride materials, have been gaining tremendous interest in recent days as potential electrocatalysts for various electrochemical reactions, including hydrogen evolution reaction (HER). MXenes are characterized by their etchable metal layers, excellent structural stability, versatility for heteroatoms doping, excellent electronic conductivity, unique surface functional groups and admirable surface area, suitable for the role of electrocatalyst/support in electrochemical reactions, such as HER. In this review article, we summarized recent developments in MXene-based electrocatalysts synthesis and HER performance in terms of the theoretical and experimental point of view. We systematically evaluated the superiority of the MXene-based catalysts over traditional Pt/C catalysts in terms of HER kinetics, Tafel slope, overpotential and stability, both in acidic and alkaline electrolytic environments. We also pointed out the motives behind the electro catalytic enhancements, the effect of synthesis conditions, heteroatom doping, the effect of surface terminations on the electrocatalytic active sites of various MXenes families. At the end, various possible approaches were recommended for a deeper understanding of the active sites and catalytic improvement of MXenes catalysts for HER.

Keywords: 2D MXene; $Ti_3C_2T_x$; water splitting; hydrogen evolution reaction; Tafel slope

check for updates

Citation: Peera, S.G.; Koutavarapu, R.; Chao, L.; Singh, L.; Murugadoss, G.; Rajeshkhanna, G. 2D MXene Nanomaterials as Electrocatalysts for Hydrogen Evolution Reaction (HER): A Review. *Micromachines* **2022**, *13*, 1499. https://doi.org/10.3390/mi13091499

Academic Editor: Nityasagar JENA

Received: 5 August 2022
Accepted: 4 September 2022
Published: 9 September 2022

1. Introduction

Increased global demand for energy is expected to be doubled by 2035 due to increased economic advancements, both in developed and developing countries [1]. At present, most of the energy demands are fulfilled by nonrenewable energy sources, such as coal, fossil fuels and natural gas. However, their usage in the near future is going to be very limited due to increased consumption, scarcity and, most importantly, the emission of greenhouse gases that have a tremendous impact on global warming [2]. Therefore, it has become a serious and urgent issue to identify alternative, renewable energy sources than can replace/limit the use of the traditional nonrenewable energy supplies for the domestic, industrial and especially transportation sector [3]. Owing to its high gravimetric energy density (140 MJ/kg), hydrogen (H_2) is considered the best energy source for transportation applications. For example, energy conversion fuel cell uses gaseous H_2 as the

fuel source [4]. In addition, gaseous H_2 is also used in a wide variety of industries and chemical reactions, such as NH_3 production and the fertilizers manufacturing sector. To meet such a high demand, in general, gaseous H_2 is produced from steam reforming and coal gasification technologies [5]. However, the most popular steam reforming and coal gasification technologies cannot solve the problem of CO_2 emission. In addition, these technologies also use high temperature for H_2 production, selective catalysts, significant amount of CO_2 along with a small quantity of impurities, such as CO (Figure 1). By no means can steam reforming and coal gasification technologies be a long-term solution for gaseous H_2 production. In addition, they aggravate the rapid depletion of fossil fuels and contribute to elevated global warming issues [6]. Therefore, the search for alternative and green energy technology for gaseous H_2 production remains a challenging and interesting task for the scientific community.

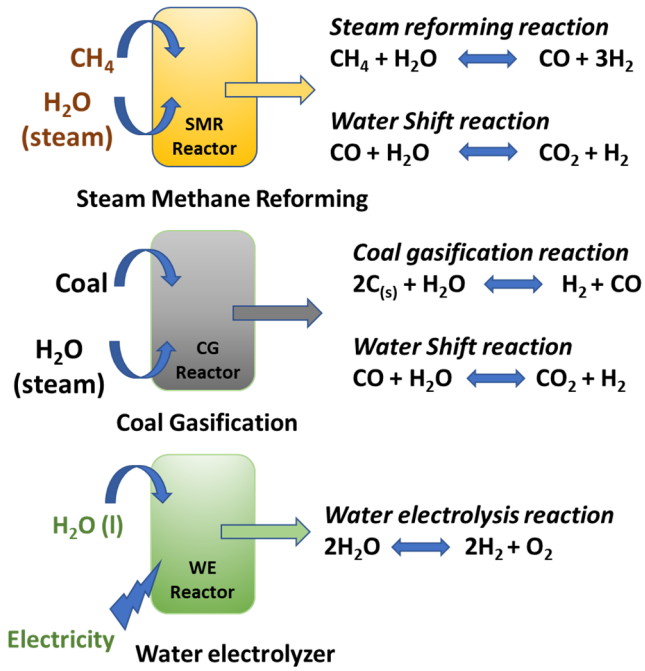

Figure 1. The three major pathways for industrial hydrogen production.

As an alternative to the traditional technologies, H_2 production by electrochemical water splitting/water electrolysis has been gaining tremendous interest recently [7]. Electrochemical water splitting into O_2 and gaseous H_2 can be the best source of H_2 energy, as it is a carbon-free technology, unlike steam reforming and coal gasification techniques. Further, water electrolysis can be performed by a variety of renewable energy resources, such as solar, wind, etc. [8]. Water electrolysis is performed by applying external voltage, which enables the decomposition of water into O_2 and H_2 gases. The O_2 gas is produced at the anodes, whereas the H_2 gas is produced at the cathodes [9]. Put simply, H_2O oxidation occurs at the anodes, which leads to O_2 evolution, referred to as an oxygen evolution reaction (OER), and H_2O reduction occurs at the cathodes, which leads to H_2 evolution, referred to as a hydrogen evolution reaction (HER). Water oxidation takes place both in acidic and alkaline electrolytes, and their respective reactions are given below.

Water electrolysis in acidic medium

$$\text{Anode: } 2H_2O\ (l) \rightarrow O_2\ (g) + 4H^+ + 4e^-\ E^\circ = 1.23\ \text{V vs. SHE}$$

$$\text{Cathode: } 4H^+ + 4e^- \rightarrow 2H_2\ (g)\ E^\circ = 0\ \text{V vs. SHE}$$

$$\text{Overall reaction: } 2H_2O\ (l) \rightarrow 2H_2\ (g) + O_2\ (g)\ \Delta E^\circ = 1.23\ \text{V},$$

$$\Delta G^\circ = +237.2\ \text{kJ}\ H_2\ \text{mol}^{-1}$$

Water electrolysis in alkaline medium

$$\text{Anode: } 4OH^- \rightarrow O_2(g) + 2H_2O + 4e^- \; E^\circ = 0.40 \text{ V vs. SHE}$$

$$\text{Cathode: } 4H_2O + 4e^- \rightarrow 2H_2(g) + 4\,OH^- \; E^\circ = -0.83 \text{ V vs. SHE}$$

$$\text{Overall reaction: } 2H_2O\,(l) \rightarrow 2H_2\,(g) + O_2\,(g) \; \Delta E^\circ = 1.23 \text{ V},$$

$$\Delta G^\circ = +237.2 \text{ kJ } H_2 \text{ mol}^{-1}$$

From the above chemical reactions, it is to be noted that the ΔG° is positive (endothermic reaction) for water electrolysis reactions, irrespective of the electrolyte media. Therefore, the surplus external potential, known as the overpotential (η), greater than the thermodynamic potential (1.23 V vs. Reversible hydrogen electrode (RHE)) needs to be applied in order to achieve water electrolysis. In addition to the applied overpotential, a suitable, active and durable electrocatalyst is also essential in order to reduce the η, both at the anodes and the cathodes of the electrolyzer cell. Traditionally, various noble metal catalysts, such as Pt, Pd, Ru, Ir and Rh, and metal oxide catalysts, such as RuO_2 and IrO_2, have been considered as excellent catalysts for OER reactions, whereas for HER, Pt-based catalysts have been considered excellent [10]. However, the high cost and scarcity of noble metals hinder their commercial applications, in addition to their low stability and aggregation during electrochemical working conditions [11]. In this regard, various low-cost, transition-metal-based catalysts have been identified and explored for both OER and HER reactions. In particular, various 2D materials, such as graphene, layered double hydroxides (LDHs), graphitic carbon nitride (g-C_3N_4), transitional metal dichalcogenides (TMDs), have been explored [12–17].

2. Mechanism of Hydrogen Evolution Reaction

The traditional HER mechanism utilizes the Volmer–Heyrovsky or Volmer–Tafel pathways, characterized by their Tafel slopes [18] (Figure 2 and Table 1).

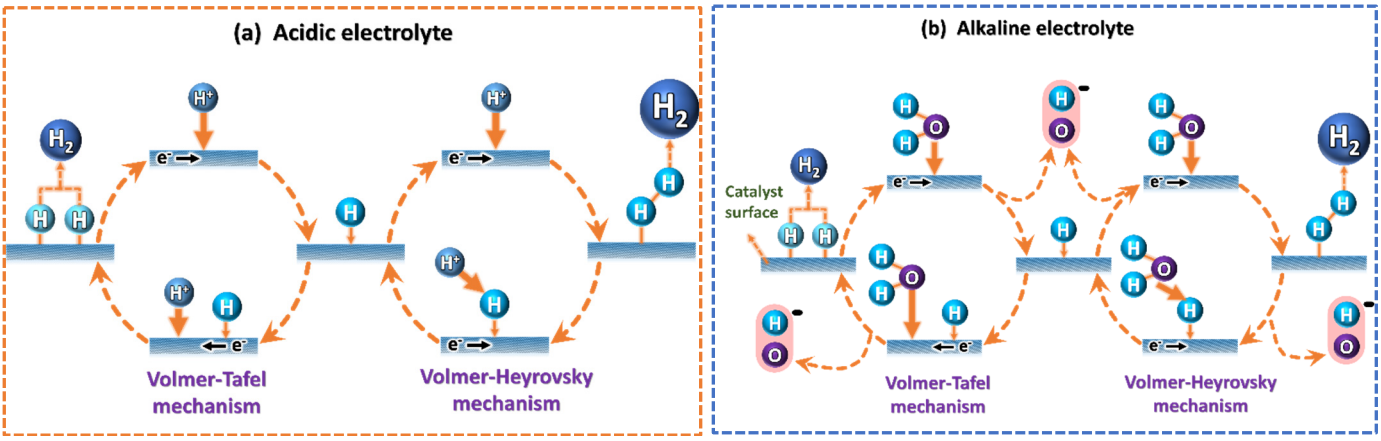

Figure 2. Schematic illustration of the hydrogen evolution reaction mechanism in (**a**) acidic and (**b**) alkaline media. HER.

Table 1. HER reactions in acidic and alkaline electrolytes and their respective Tafel slopes.

Reaction	Acidic Medium	Basic Medium	Tafel Slop
Volmer step	$H^+ + e^- \rightarrow H^*$	$H_2O + e^- \rightarrow H^* + OH^-$	120 mV dec^{-1}
Heyrovsky step	$H^* + H^+ + e^- \rightarrow H_2$	$H^* + H_2O + e^- \rightarrow OH^- + H_2$	40 mV dec^{-1}
Tafel step	$2H^* \rightarrow H_2$	$2H_2O + 2e^- \rightarrow 2OH^- + H_2$	30 mV dec^{-1}

In the acidic medium, HER starts with the adsorption of atomic hydrogen onto the electrode surface by the reduction in H^+ with the help of an electron. In the second step, another H^+ is reduced with the help of an electron, together combining the previously adsorbed atomic H to form H_2. Alternatively, H_2 may also form by combining two adsorbed atomic H, directly [19]. In total, HER is a two-electron transfer reaction, as shown below. In the alkaline medium, HER begins with water reduction to H* and OH^-. In the second step, another water molecule dissociates to H* and OH^-; simultaneously, two atomic H* combine to form H_2.

As per the chemical reactions stated above, the adsorption of hydrogen (H^*_{ads}) is an important step, and the Gibbs free energy (ΔG_H*) of hydrogen adsorption is the criterion/rate determining step for the initiation of the reaction. The ΔG_H* varies depending on the type of metallic electrocatalyst. An ideal electrocatalyst is one with the best compromise between the adsorption and desorption energies. Too strong adsorption leads to Heyrovsky/Tafel as the rate determining reaction, whereas weaker adsorption leads to a Volmer reaction as the rate determining step. Figure 3 shows the Sabatier volcano plot (ΔG_H* vs. their exchange current densities) for the adsorption and desorption of H on various metallic surfaces [20]. It can be seen that most of the Pt group/noble metals occupy the highest position in the volcano plots with the optimized ΔG_H* and high exchange current densities. This indicates that all the noble metal catalysts and Pt perform excellent HER kinetics, with nearly zero ΔG_H* values. While the metallic catalysts on the left of the Pt group metals adsorb too strongly ΔG_H* < 0, the metallic catalysts on the right of the volcano plots adsorb too weakly ΔG_H* > 0, affecting the desorption and adsorption of the H atoms, thus ultimately affecting the overall HER kinetics.

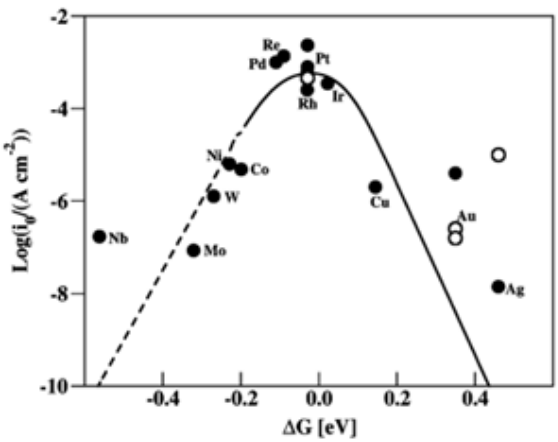

Figure 3. HER Volcano plot for metals (Reprinted with permission from Ref. [15]. Copyright 2010, American Chemical Society).

3. Effect of Support Materials on the HER

In addition to the type of metal as an active site (as shown in Figure 3), the kinetics of HER is also influenced by the support material on which the metallic nanoparticles are dispersed. Support materials plays a key role in improving HER catalytic activity in a number of ways. The support material helps in the even distribution on the nanoparticles, thereby mitigating nanoparticle aggregation and enhancing the electrochemical active surface area of the nanoparticles [21]. Catalyst support acts as a mediator for the electron transport pathway into/out of the catalyst. For any material to be considered as catalyst support, it should possess some prerequisites, such as (i) a suitable surface area for the dispersion of nanoparticles, (ii) high electronic conductivity to minimize the ohmic losses, (iii) electrochemical stability (corrosion resistance), (iv) good metal-support adhesion, (v) suitable porosity. Therefore, the type of catalyst support highly influences the kinetics and stability of the catalyst. In general, carbon materials, such as carbon black, carbon nanofibers, graphene, carbon nanotubes, heteroatom (N, B, P, S, F, etc.) doped carbons,

are used as support materials owing to their balanced electronic conductivity, surface area and porosity [22–26]. Nonetheless, carbon material materials are subjected to severe degradation (carbon corrosion) in the acidic and alkaline electrolytes [27]. Carbon corrosion leads to a loss of electronic contact, detachment of the supported nanoparticles and aggregation of nanoparticles, thereby reducing the kinetics of HER over longer periods of operation [28]. In this regard, various non-carbon supports have been explored as excellent and corrosion-resistant catalyst supports, such as transition metal oxides/carbides/nitrates. In comparison with traditional carbon-based supports, strong metal-support interactions between non-carbon supports and metallic nanoparticles have been found and well established by different researchers [29,30].

Novel 2D layered transition metal carbides/carbonitrides/nitrides, popularly known as MXenes, discovered by Drexel University, Philadelphia, United States researchers in 2011, have been gaining remarkable interest as support material for various electrochemical reactions, such as oxygen reduction reaction [31], methanol/ethanol oxidation reaction [32], nitrogen reduction reaction [33], sensors [34], carbon dioxide reduction reaction, supercapacitors [35], OER and HER [36], photocatalytic degradation of organic pollutants [37], improved mechanical and tribological properties [38], photooxidative performance for heavy metal removal [39] and hydrodeoxygenation reactions [40]. In this review article, we emphasized the importance of MXenes as catalyst/support material for HER catalysis. We briefly discussed the structure of MXenes, surface chemistry, stability and HER catalytic properties of MXenes-based electrocatalysts, followed by a summary of recent advances in MXenes electrocatalysts and HER kinetics, both from the theoretical and experimental point of view. Finally, we also proposed future research perspectives and directions for catalytic activity improvements.

4. MXene—Structure

MXenes are synthesized from their parent bulk material $M_{n+1}AX_n$, where M = transition metal, A is an A-group element, and X is C and/or N, n = 1, 2, 3. These $M_{n+1}AX_n$ materials are then simplified with the term MAX. The bulk MAX materials are structurally hexagonal, where the layers of the edge-shared M6X-octahedra are interleaved with layers of "A" elements, which are located at the center of the trigonal prisms. The "n" value indicates the number of "M" layers separating the A layers. The MAX phases possess unique properties, such as strong, mixed metallic-covalent M-X bonds on one side and weaker M-A bonds on the other sides. This unique structure enables breaking the weaker M-A bonds and maintaining the strong M-X bonds, selectively. Apparently, the MXenes are synthesized by treating the bulk parent material MAX with strong acids, such as NH_4HF_2, LiF + HCl and HF, which selectively etches the A layer to produce MXenes ($M_{n+1}X_nT_n$). MXenes are a type of layered materials composed of transition metal (TM) carbide/nitride/carbonitride, represented by an empirical formula $M_{n+1}X_nT_n$, (M = TM, X = carbon or nitrogen, T = -OH, -O and -F and n = integers 1, 2, 3) [41–43]. MXenes have three representative structures, namely, M_2XT_x, $M_3X_2T_x$ and $M_4X_3T_x$, with *n* layers of X elements covered by n + 1 layers of M [44]. There have been a number of review articles published in recent times describing the structure and properties of MAX phases and $M_{n+1}X_nT_n$; they can be found in References [45–47] for detailed information.

5. Surface Chemistry and Stability of MXenes

The surface of MXenes offers a wide variety of functionalities (-F, -OH, -O, etc.) that are originated from the synthesis process, especially during the HF etching of the MAX phase. Various DFT calculations suggest that MXenes show a significant gain in negative formation energies after HF treatment, which indicates the formation of strong bonds between the surface of the M layer and chemical functionalities [48] by the following reactions.

$$Ti_3AlC_2 + 3HF \rightarrow AlF_3 + 3/2\ H_2 + Ti_3C_2$$

$$Ti_3C_2 + 2H_2O \rightarrow Ti_3C_2(OH)_2 + H_2$$

$$Ti_3C_2 + 2HF \rightarrow Ti_3C_2F_2 + H_2$$

Recent studies revealed that some of the -OH terminations eventually undergo dehydrogenation reaction to form -O termination by the following reaction [49].

$$Ti_3C_2(OH)_2 \rightarrow Ti_3C_2O + H_2O$$

There are many ways these surface functionalities affect the properties of MXenes, such as hydrophilicity/hydrophobicity, stability and electronic conductivity [50–52]. The thermodynamic stability of MXenes highly depends on the type of surface functional groups and follows the order of $Ti_3C_2O_2$ > $Ti_3C_2F_2$ > Ti_3CH_2O > $Ti_3C_2H_2$ [53]. Further, long storage of MXenes also allows the structural phase transformations. A gradual oxidation of MXenes starts at the F-terminations into oxy-fluorides, leading to increased -O terminations along with the decreased -F terminations [54]. MXenes are also very sensitive toward oxygen, H_2O and temperature. In the presence of O_2, MXenes undergo structural phase transformations. For example, the colloidal $Ti_2C_2T_x$ stored in an open atmosphere gradually transforms into TiO_2, even at room temperature. Further, the smaller the flake size of $Ti_2C_2T_x$, the faster the transformation. Therefore, it is always recommended that MXenes are stored in a colloidal form in dark and under low temperatures or as powdered MXenes in the inert atmosphere to ensure their intact structural stability [55]. Higher temperature is also known to have a definite effect on the structural phase of MXenes. A temperature of 200 °C and below is considered a safe temperature, without any disturbance to the layered $Ti_2C_2T_x$ MXenes structure. Higher temperatures and oxygen atmosphere lead to the transformation of $Ti_2C_2T_x$ to the anatase TiO_2. In contrast, heat treatment in reducing atmospheres, such as H_2/Ar, H_2/N_2, H_2, is found to induce very minimal structural change in MXenes [56].

The electronic conductivity of MXenes is highly dependent on the density of the surface functional groups; the higher the density, the lower the electronic conductivity. Because the introduction of surface functional groups is inevitable with etchants such as HF, a careful optimization of the synthesis conditions is very important for applications where the electronic conductivity of the materials matters. For this purpose, there have also been studies to tailor the electronic properties of MXenes by tailoring the terminations and intercalation of the other ions into MXenes structures. One of the best approaches is to post treat the MXenes after the etching process. For example, the post treatment of MXenes by KOH or CH_3CO_2K, is found to reduce the -F terminations [57]. The other way is to perform a post heat treatment of MXenes in H_2 atmosphere, which greatly reduces the -O or -OH terminations in the MXenes by the following equation [58].

$$Ti_3C_2(O)_2 + 2H_2 \rightarrow Ti_3C_2 + 2H_2O$$

Recently, vacuum annealing of MXenes was found to be one of the best ways to defunctionalize the surface groups and restore the electronic conductivity of Mxenes [59]. Therefore, choosing the right etchant, heat treatment temperatures, drying and storage of MXenes are very important to maintain their intact structure and stability for relevant applications.

6. MXene-Based Electrocatalysts for the HER

In general, high-cost precious metals, such as Pt and R/C, are used for HER due to their excellent kinetics and stability. However, high prices and low abundance are the major obstacles for the commercial use of precious metals. Therefore, research has been devoted to developing cheap electrocatalysts composed of non-precious metals/carbons, such as transition metal phosphides, nitrides, sulfides, oxides, and even electrocatalysts with no metal—so-called

metal-free catalysts—have been developed [60–64]. However, there are still problems with non-precious-metal catalysts, such as poor electronic conductivity and low stability. In this regard, MXenes could hold potential properties, such as (a) their excellent metallic conductivity (up to 10,000 S cm^{-1}), which facilitates faster charge-carrier transfer during HER that guarantees the high electronic density around the active sites; (b) structural integrity due to a layered structure; (c) corrosive resistance properties due to Ti, Mo, V in combination with C and N, which guarantee long-term stability in aqueous electrolytes; (d) intrinsic hydrophilicity, which ensures adequate contact with water molecules; (d) a large surface area to host the guest metal nanoparticles and expose maximum surface area for a reaction [27].

In addition, MXenes offer great stability over traditional Pt/C catalysts. In general, Pt/C catalysts are prone to undergo corrosion under acidic and alkaline conditions, which leads to Pt nanoparticle agglomeration. The traditional carbon, i.e., the Vulcan carbon, used as support for Pt nanoparticles is known to be extremely sensitive to carbon corrosion due to its poor crystallinity [65]. Further, it is well established that the interaction between the metal and carbon support is weaker in Pt/C [66]. In this regard, MXenes, as catalysts or catalyst supports, could offer potential stability due to the high crystallinity of MXenes and adequate bonding between C and M, and a lower density of unstable surface functionalities compared to Vulcan carbons. For example, Ti-based MXenes $Ti_3C_2T_X$ bond strongly between Ti and C, mitigating the corrosion of carbon. The Ti in the catalyst provides ample durability under oxidative and acidic environments. Further, the strong bonding between Ti and C generates unique electronic properties at the Ti-C heterojunctions. In addition, the -F termination has been proven to be highly stable under a wide range of operating potentials; therefore, it could prevent the corrosion and aggregation of metallic nanoparticles, thus offering long-term stability compared to the traditional Pt/non-Pt carbon catalysts. Considering the above-mentioned advantages, various MXenes-based electrocatalysts have been synthesized using various strategies, such as modifying the surface terminal groups, metal doping, metal nanoparticles deposition and hybridization of MXenes with other carbon and non-carbon 2D materials. This review summarizes the recent developments of MXene electrocatalysts for HER, both from the theoretical and experimental research point of view.

6.1. Theoretical Perspectives on Kinetics and HER Mechanism of MXenes

Ab initio theoretical analysis has been gaining special attention in recent years, especially the density functional theory (DFT) calculations. For energy conversion reactions, DFT calculations help in identifying and predicting the active electrocatalysts together with the possible reaction mechanism and pathway based on the Gibbs free energy diagram, formation energy and volcano plots [67]. This section highlights the theoretical studies on MXene electrocatalysts. Bai et al. [68] investigated the HER activity of 20 different MXenes of two different families of MXenes, namely M_2NO_2, M_2CO_2 (M = Sc, Ti, V, Cr, Zr, Nb, Mo, Hf, Ta and W), using the Fermi abundance model. An ideal catalyst should have zero (ΔG_H). When the H coverage analysis (25%) reveals M_2NO_2 (M = M = Ti, V, Cr, Nb and Ta) as the catalyst, the ΔG_H value is between −0.25 and 0.25 eV. In particular, Ti_2NO_2 and Nb_2NO_2 show close ΔG_H values with those of Pt (1 1 1), i.e., 0 eV, suggesting that Ti_2NO_2 and Nb_2NO_2 MXenes exhibit close HER activity to that of Pt, whereas M_2NO_2 (M = Sc, Zr, Mo, Hf and W) show high ΔG_H values, suggesting their low intrinsic HER activity. In the case of the carbide type of M_2CO_2 MXenes, the Ti_2CO_2 and W_2CO_2 catalysts show optimal ΔG_H (~0.12 eV). Similar observations are also drawn for the exchange current densities vs. ΔG_H volcano plots. Among all the catalysts, the Ti_2NO_2 and Nb_2NO_2 catalysts occupy the top of the curve, exhibiting larger exchange current densities (10^{-17} A/site) than the Pt (1 1 1) catalyst (10^{-18} A/site). In terms of the HER mechanism, Ti_2NO_2 and Nb_2NO_2, the Volmer–Heyrovsky mechanism is found to be preferred.

Huang et al. [69] investigated the transition metal carbonitrides M_3CN type of MXene for ΔG_H, and the electronic charge transfer on the surface terminated and un-terminated for HER kinetics. A detailed analysis reveals that Ti- and Nb-based MXenes (Ti_3CNO_2 and Nb_3CNO_2) show excellent HER kinetics. The calculated ΔG_H values are found to be negative (−1.173 to −0.709 eV) for all the investigated M_3CN types. Further, the H adsorption is stronger on the N side of the MXene than on the C side. Further, the O-terminations are found to be beneficial for enhancing the HER, as can be seen from the smaller $\Delta G_H < 0.2$ eV for Nb_3CNO_2 and Ti_3CNO_2, especially with Nb_3CNO_2. Further, the volcano plots suggest that Nb_3CNO_2 positions close to Pt. Jin et al. [70] investigated 2D ordered double transition-metal carbides (MXenes) with the chemical composition of $M_2'M''C_2T_x$ and $M_2'M_2''C_3T_x$; M′ and M″ with two different metals (M′ = Cr, V, Ti, or Nb; M″ = Nb, Ta, Ti or V; and T = O and/or OH) by a detailed DFT analysis. A total of 18 different carbide species of different combinations were investigated, of which a double transition-metal carbide $Mo_2NbC_2O_2$ showed the lowest overpotential. The volcano plots revealed that the HER performance of the double TM carbide MXenes strongly depends on the type of surface metal, and based on the performance, the investigated catalysts were grouped under three different categories, i.e., (i) O-terminated Mo-, Ti-based Mxenes with moderate adsorption for hydrogen species, corresponding with higher HER activity; (ii) O-terminated V- and Cr-based MXenes with strong adsorption for hydrogen species, corresponding with lower HER activity; (iii) MXenes with Ta and Nb with too weak hydrogen adsorption energies, corresponding with their unsuitability as HER catalysts. Further, in the case of double layer transition-metal carbide MXenes, it is observed that the type of metal in the inner layer has no significant effect on the HER activity. Further, it is found that -O, -OH and -F terminations help more in hydrogen adsorption than the bare double TM MXenes. Figure 4 shows the optimal 18 types of MXenes with the ideal overpotential of less than 0.2 V, derived from the DFT analysis.

In another DFT study by Zeng et al. [71], they investigated 64 different types of double transition metal carbonitrides $M'_2M''CNO_2$ (M′ = Ti, V, Cr, Zr, Nb, Mo, Hf, Ta; M″ = Ti, V, Cr, Zr, Nb, Mo, Hf, Ta). Among the 64 types, 11 types of $M'_2M''CNO_2$ catalysts were found highly active in terms of Pt; regarding stability, Ti_2NbCNO_2, Mo_2TiCNO_2 and Ti_2VCNO_2 were found to be highly stable. The screenings of the most stable catalysts for HER are based on the Gibbs free energy calculations, as per the flow chart given in Figure 5 volcano plots. Similar to the earlier study [70], the type of metal on the outer layer was more important for enhancing the HER activity than the inner metals; especially when the outer layer was Ti or Nb, the HER activity was found to be higher than the other metals. Furthermore, the MXenes $M'_2M''CNO_2$ with the C side are found to be optimum for H adsorption compared to the N side. Further, the volcano plots indicate that both on the C side and the N side, together, the 11 types of $M'_2M''CNO_2$ catalysts show the best HER activity, with the best pick of the $M'_2M''CNO_2$ catalyst with ΔG_H values close to 0.003 eV, which is the best catalyst with almost zero ΔG_H, showing its potential as an extraordinary HER catalyst. It is important to understand the formation energy and stability of the investigated MXenes due to the fact that the theoretically screened catalysts need to be able to synthesize in the laboratory conditions. The stability or formation energy analysis ($E_{formation}$) reveals that of the 11 best screened catalysts, Ti_2NbCNO_2, Ti_2VCNO_2 and Mo_2TiCNO_2 catalysts showed negative formation energies, indicating that these types of $M'_2M''CNO_2$ are thermodynamically stable and can be synthesized experimentally. In addition to the traditional DFT studies, recently, machine-learning and high-throughput studies have been employed to screen and identify various possible MXenes for HER [72,73]. In summary, the DFT analysis of the single/double layered transition metal carbides/nitride reveals that there are tremendous opportunities to explore the different types and combinations of MXenes experimentally based on the DFT clues.

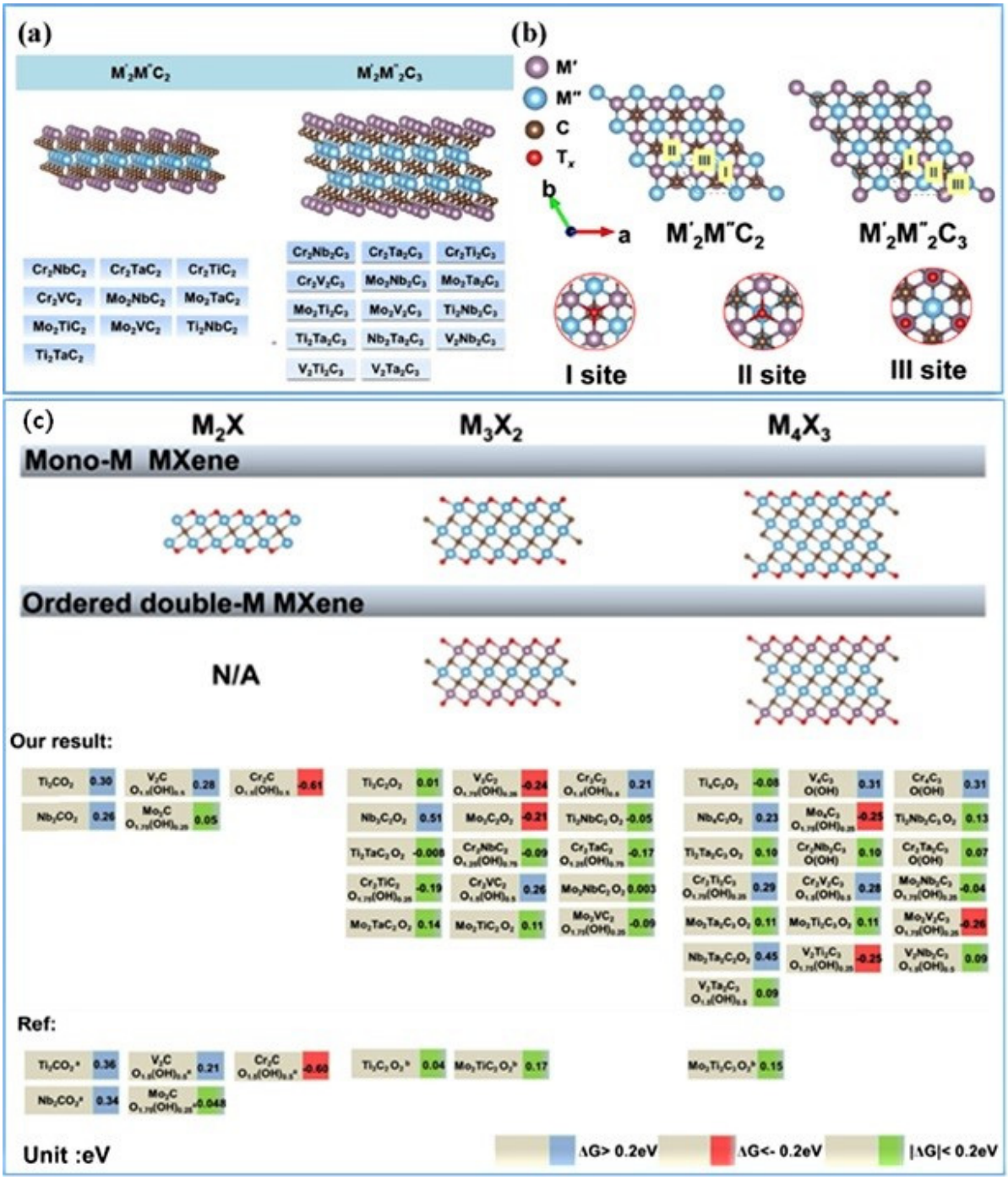

Figure 4. (**a**) List of ordered double TM carbides investigated in this work. (**b**) Atomic structure of M2′M″C2 and M2′M2″C3 viewed from the top. The "I site", "II site" and "III site" represent three high-symmetry adsorption sites for -O and -OH termination on the outermost layer. Color code: M′ (blue), M″ (purple), C (brown) and Tx (red). (**c**) Calculated Gibbs free energy (in eV) for single M2′C, M3′C2 and M4′C3 (M′ = Ti, V, Cr, Nb and Mo) carbide MXenes and corresponding values for investigated double TM MXenes. (Reprinted with permission from Ref. [70]. Copyright 2020, American Chemical Society).

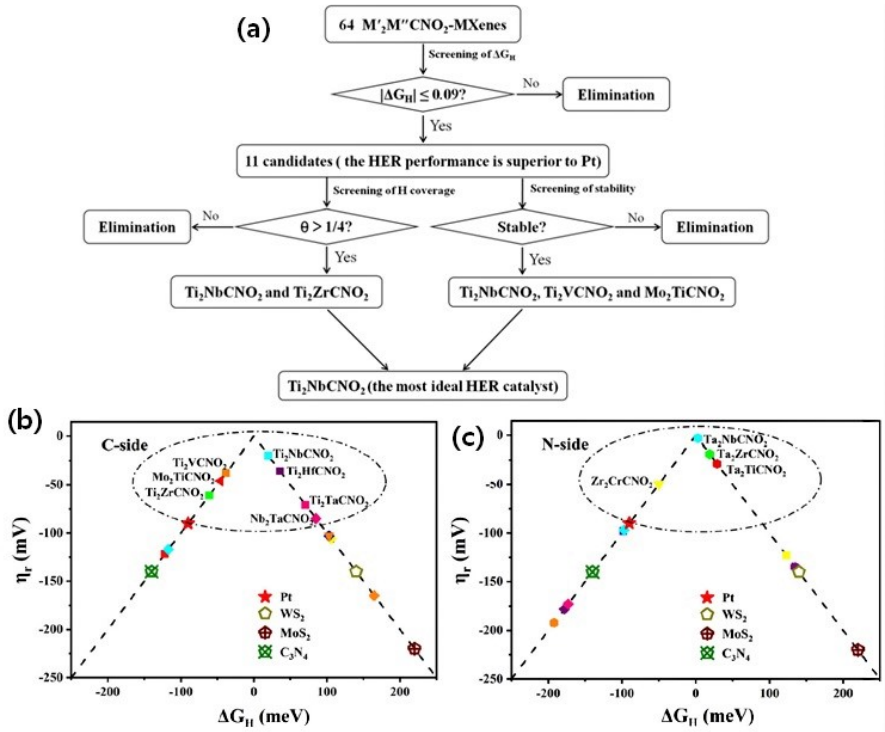

Figure 5. (**a**) Screening workflow. The screening process of HER catalysts from 64 $M'_2M''CNO_2$-MXenes. The volcano plotted for all 64 $M'2M''CNO_2$-MXenes of (**b**) C side (**c**) N side. The different shapes represent different M′, and different colors represent different M″ (red, orange, yellow, green, cyan, blue, purple and pink represent Ti, V, Cr, Zr, Nb, Mo, Hf and Ta, respectively). Adapted from Ref. [71], (Open Access).

6.2. Experimental Perspectives on Kinetics and HER Mechanism on MXenes

6.2.1. Pristine MXenes for HER

Kumar et al. [74] investigated the HER activity of the pristine MAX phase materials of seven different types, namely, Ti_2AlC, Ta_2AlC, Ti_2SnC, Ti_3SiC_2, V_2AlC, Mo_2TiAlC_2 and Cr_2AlC in 0.5 M H_2SO_4. The MAX phases of the respective compounds are used as such without etching of the M layer to understand the intrinsic HER activity of MXenes (Figure 6a,b). Half-cell studies indicate that among the seven types of MXenes, double layer MXene Mo_2TiAlC_2 showed enhanced HER activity followed by V_2AlC. The overall order is as follows: $Mo_2TiAlC_2 > V_2AlC > Cr_2AlC > Ti_2SnC > Ti_2AlC > Ta_2AlC > Ti_3SiC_2$. This order clearly indicates that the MXenes HER activity is based on the type of surface metal atoms. Further, the double metal atom layer MXenes seem to outperform single atom layer MXenes, as evidenced by the higher HER activity of Mo_2TiAlC_2 than the V_2AlC and traditional Ti_2AlC. In the Mo_2TiAlC_2, the sandwiched Ti atoms between the two layers of Mo, which are, in turn, adjacent to the detachable Al, generate the potential stacking structure made up of Mo-Ti-Mo-Al-Mo-Ti-Mo. The exposure of the Mo atoms sandwiched by Ti generates unique surface and electronic properties compared to traditional Ti_2AlC. This unique structural arrangement is found to be the responsible factor for the enhanced HER activity of the Mo_2TiAlC_2 compared to the other types of MXenes. The Mo_2TiAlC_2 showed an overpotential of −0.57 V vs. RHE, which was higher among all the other types of MXens. This clearly indicates that MXenes composed of Mo, Ti, V are one of the best MXenes catalysts for HER activity.

6.2.2. Effect of Surface Functionalization of MXenes for HER

It is well known that the etching of the parent MAX phase inevitably introduces various functional groups to MXenes, which includes -F, -O and -OH. These surface functional groups are known to enhance the stability and metal support interaction for several

electrochemical reactions, such as ORR, OER and HER. DFT studies described in the above sections also evidenced that the surface terminated/functionalized MXenes' lower HER overpotential than the bare MXenes. Li et al. [75] investigated the effect of F-terminated nanosheets of MXenes on HER and found a direct relationship with the content of -F. In a comparison study, the Ti_2CT_x with less -F termination and the etched Ti_2CT_x are reacted with KOH to remove the -F terminations and to remove the -O/-OH functional groups. The Ti_2CT_x is further annealed at high temperatures (200 °C for 2 h). The HER analysis of the three catalysts shows that the Ti_2CT_x terminated with -F shows better ORR activity, indicating that the presence of -F terminations is quite significant for HER activity. The Ti_2CT_x devoid of the -O/-OH functional groups did not show significant change in the overpotential, whereas alkalized Ti_2CT_x showed a drastically reduced overpotential, clearly indicating the significance of -F terminations. F-surface termination not only affects pristine MXenes' HER activity; it also affects the supported metal nanoparticles. Zhang et al. [76] investigated the effect of -O/-OH and -F terminated Pd-supported Nb_2CT_x on HER activity. From the DFT studies, it was revealed that Pd_4 clusters absorbed on Nb_2CF_2-F_v and Nb_2CO_2-O_v supported the binding energy of −3.3 eV and −3.6 eV. On the contrary, Bader charge analysis revealed that there were 0.32 and 0.03 e^- transferred between Pd_4 and Nb_2CF_2-F_v and Nb_2CO_2-O_v, respectively (Figure 6c–e). Experimental HER analysis also revealed that the HER activity of the Pd_4-supported Nb_2CF_2-F_v was strongly dependent on the surface functional groups. The obtained HER η of Pd/Nb_2C-HF, Pd/Nb_2C-H_2SO_4 and Pd/Nb_2CHNO_3 were 34, 43 and 46 mV. The HER performance of the catalysts decreased either with increased -O content or decreased -F contents, clearly suggesting that the HER kinetics are dependent on the content and type of surface functional groups. The optimized Pd/Nb_2C-HF catalyst also showed excellent stability, both in chronoamperometric and potential cycling analyses (Figure 6f,g).

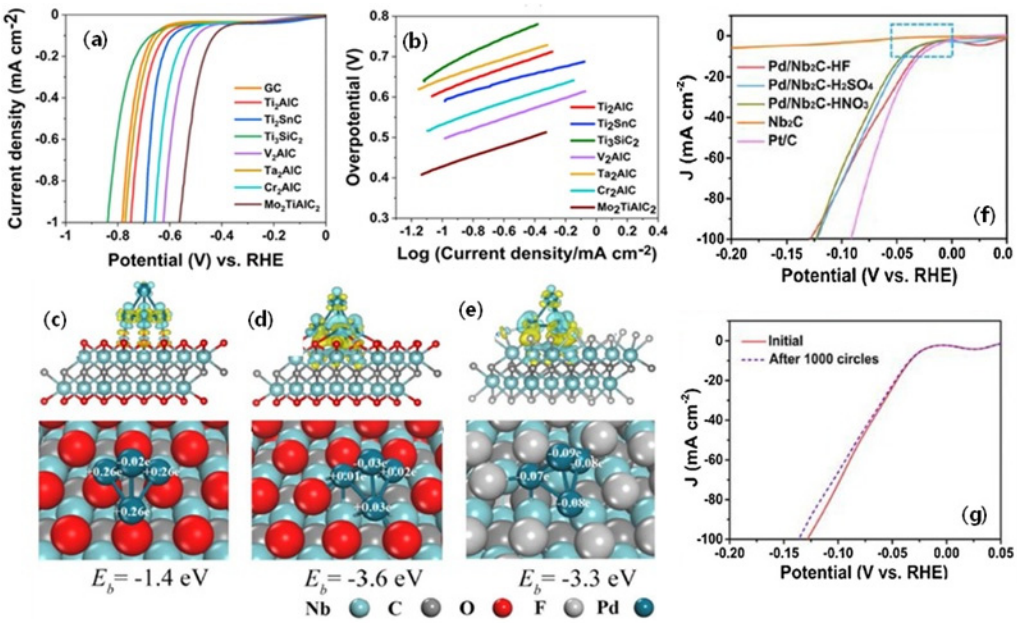

Figure 6. (**a**) Linear sweep voltammograms of GC, MAX phases at a scan rate of 5 mV s^{-1}. (**b**) Tafel plots of MAX phases (Adapted from Ref. [74], Open Access). Charge density differences, binding energies, and Bader charges of Pd_4 cluster supported with O-terminated Nb_2C (**c**), O-terminated Nb_2C with one O vacancy (**d**), F-terminated Nb_2C with one F vacancy (**e**), cyan (yellow) isosurfaces indicate depletion (addition) of 0.005e/$Å^{-3}$. The cyan, gray, red, silver, deep-blue spheres represent the Nb, C, O, F and Pd, respectively. (For interpretation of the references to color in this figure legend, the reader is referred to the web version of this article). Electrochemical performance of the supported nano catalysts (**f**) HER polarization curves (**g**) Polarization curves Pd/Nb_2C-HF before and after 1000 cycles testing (Reprinted with permission from Ref. [76] Copyright, Elsevier).

6.2.3. Heteroatom Doped MXenes for HER

It is believed that doping of the heteroatoms, such as N, S and P, etc., with the MXenes enhances the chemical, electrochemical and electronic properties, which are beneficial for HER reactions. Doping of the heteroatoms not only creates defects but also exerts a synergistic interaction with the deposited metal nanoparticles for enhanced HER kinetics. Yoon et al. [77] successfully doped N into the Ti_2CT_x by the process of nitridation by using sodium amide ($NaNH_2$) as the source of N at the temperature of 500 °C. The XPS analysis clearly revealed the successful introduction of N by the appearance of Ti-N_x bonding states. It is observed that N doping with the Ti_2CT_x changes the electronic properties, which results in increased HER activity of N-Ti_2CT_x compared to pristine Ti_2CT_x. At the current density of 10 mA cm^{-2}, the N-Ti_2CT_x exhibits the η of −215 mV, whereas the pristine N-Ti_2CT_x shows the η of −645 mV vs. NHE, which represents a more than three-fold enhancement over the pristine N-Ti_2CT_x. In another study, Le et al. [78] synthesized N-doped $Ti_3C_2T_x$ by using NH_3 heat treatment at 800 °C (Figure 7a). The SEM images show a sheet-like structure of N-doped Ti3C2Tx along with the successful doping of N ascertained from the SEM elemental mapping analysis (Figure 7b,c). It is found that N doping with $Ti_3C_2T_x$ introduces different bonding possibilities, such as N-H, Ti-N and O-Ti-N. In addition to the Ti-N configurations, it is observed that N-H and O-Ti-N also change the electronic properties of $Ti_3C_2T_x$, which leads to the optimized ΔHad* value close to zero (0) eV by DFT calculations, indicating the potential of N-doped $Ti_3C_2T_x$ as excellent HER catalyst. In support of the DFT calculations, the N-doped $Ti_3C_2T_x$@600 catalyst showed the η of 198 mV at 10 mA cm^{-2}, several orders higher than the pristine $Ti_3C_2T_x$ catalyst. The enhanced HER activity was associated with the synergistic effect on the electronic modification of the $Ti_3C_2T_x$ due to N-doped active sites, such as N-H, Ti-N and O-Ti-N. Through a detailed XPS analysis, it was revealed that among the three possible N-doped active sites, N-H and O-Ti-N were found to be more important than Ti-N due to the fact that the % Ti-N in $Ti_3C_2T_x$@800 was higher than $Ti_3C_2T_x$@600; the former HER activity was less than the latter (Figure 7d,e). Further, higher calcination temperature was found to affect the % of N-H and O-Ti-N, as seen from the lower % of them in $Ti_3C_2T_x$@800 than in $Ti_3C_2T_x$@600. Therefore, it is reasonable to conclude that the optimized calcination temperature of 600 °C is essential for the optimized HER activity.

Han et al. [79] recently developed a simple ultrasonication strategy to precisely control the N doping with the $Ti_3C_2T_x$ catalyst. The N doping is performed by ultrasonicating $Ti_3C_2T_x$ in the presence of a mixture of ammonia and sodium borohydride solution at the temperature of 35 °C. With no further heat treatment, the N-doped $Ti_3C_2T_x$ is obtained. It is believed that ultrasonic waves create tremendous defects for the adsorption of NH_3 molecules. During ultrasonication, the removal of oxygen-containing functionalities provides the space for the doping of N atoms to create various N-containing functionalities, such as C-NH_2, C-NH, Ti-N and Ti-NH_2. Therefore, N doping occurs at the thermodynamically and kinetically unstable -O functional groups removed by the long ultrasonication process at 35 °C. SEM revealed that long-term sonication did not change the layered, structural stability of $Ti_3C_2T_x$. When electrochemically evaluated for HER, the pristine $Ti_3C_2T_x$ catalyst showed a large η of 575 mV, whereas N-$Ti_3C_2T_x$-35 showed excellent enhancement, with a η of 163 mV. The Tafel slope analysis revealed a slope of 69 mV dec^{-1}, indicating that the HER reaction mechanism in N-$Ti_3C_2T_x$-35 is a type of Volmer–Heyrovsky reaction. Impedance spectroscopy also revealed the lowest resistance for N-$Ti_3C_2T_x$-35 due to the doping of N, which helped in faster charge transfer during the electrochemical reactions. In addition to the enhanced HER activity, N-$Ti_3C_2T_x$-35 also showed excellent stability, with almost zero degradation in the overpotential after 24 h, and a stable current with almost no loss in potential for 35 h. In summary, the doping of N with the $Ti_3C_2T_x$-based MXenes is proved to be beneficial for enhanced HER kinetics and stability.

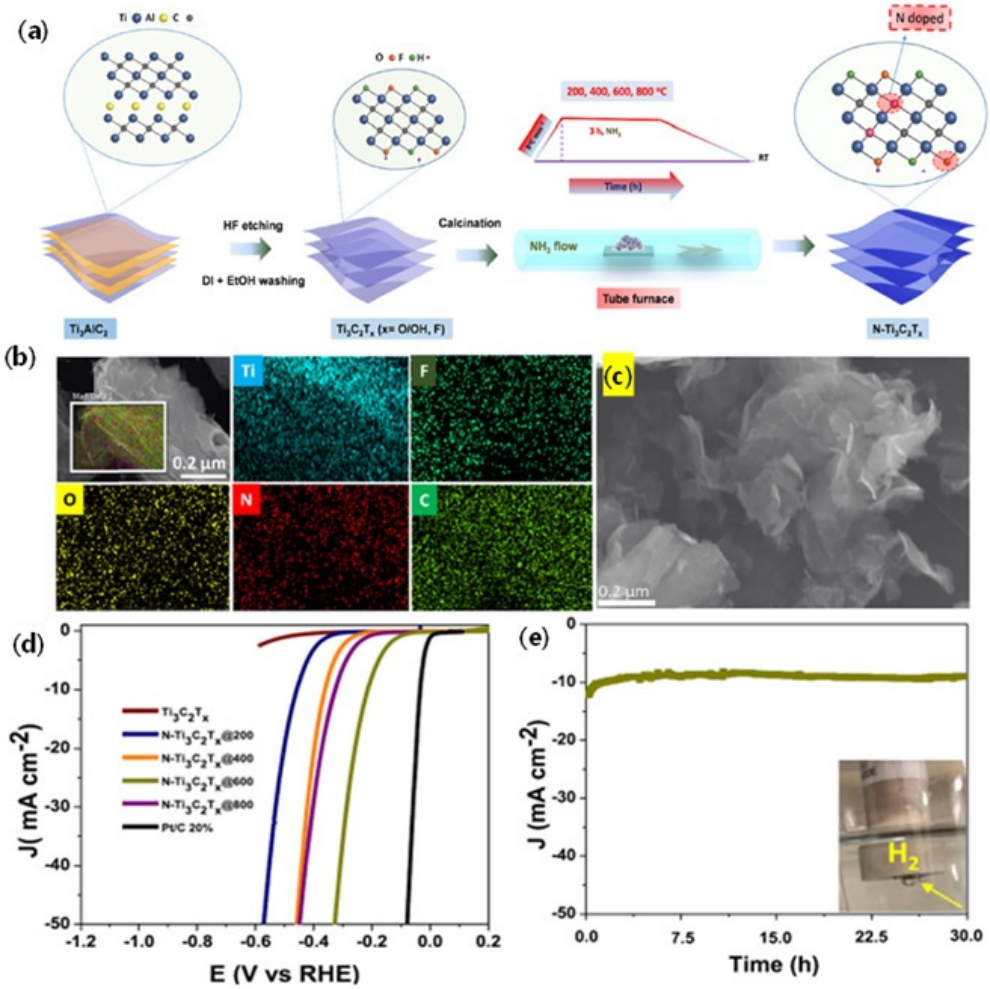

Figure 7. (**a**) Illustration of synthesis of N-doped MXene from the Ti_3AlC_2 MAX phase. (**b**) SEM–EDX elemental mapping of N-$Ti_3C_2T_x$600 and (**c**) SEM image of delaminated N-$Ti_3C_2T_x$@600. (**d**) HER polarization curves of $Ti_3C_2T_x$ and a series of different N-doped $Ti_3C_2T_x$ catalysts. (**e**) Test at a constant overpotential of −0.19 V (inset: photo of a rotating disk electrode (RDE) with the produced H_2 bubbles on its surface). Reprinted with permission from Ref. [78]. Copyright 2019, American Chemical Society.

6.2.4. Pt/$Ti_3C_2T_x$-Based MXenes for HER

In general, Pt/C catalysts with Pt wt% ~20 are used in the current technology and as a comparative benchmark for assessing the other types of catalysts. However, 20 wt% of Pt is still high for practical application due to its high cost. Efforts have been undertaken to reduce the loading of Pt several-fold while at the same time maintain the high HER kinetics. Zhnag et al. [80] investigated the HER activity of low Pt loading supported on $Ti_3C_2T_x$. The Pt deposition was carried out by the atomic layer deposition (ALD) technique. Pt NPs of 2 nm in diameter are deposited by controlled ALD cycles, and the obtained Pt/$Ti_3C_2T_x$ of Pt wt% 1.7 catalyst showed almost equal HER activity to that of Pt/C 20 wt%. The TEM images clearly show that the Pt nanoparticles are homogeneously dispersed on the $Ti_3C_2T_x$ support with a lattice fringe of 0.23 nm, corresponding to Pt (1 1 1). The 40Pt-TBA-$Ti_3C_2T_x$ catalysts showed an overpotential of 67.8 mV@10 mA cm^{-2}, whereas it was 64.2 mV for Pt/C catalysts, a mere 3.6 mV inferiority. This indicates that the low loading of Pt by ALD could deliver similar HER activity as that of a high loading of Pt/C. The high HER activity of 40Pt-TBA-$Ti_3C_2T_x$ is further ratified by measuring the ECSA, which show a calculated value of 16.6 and 16.6 μF cm^{-2}, which is almost close to the Pt/C catalyst (19.7 μF cm^{-2}), despite the 18-times-lower Pt loading due to the fact the ALD

gives homogeneous dispersion compared to the traditional wet impregnation of Pt, which results in agglomerations. The 1.7 wt% Pt-$Ti_3C_2T_x$ catalyst showed excellent stability over 3000 cycles, with no visible change in the voltage (Figure 8a,b).

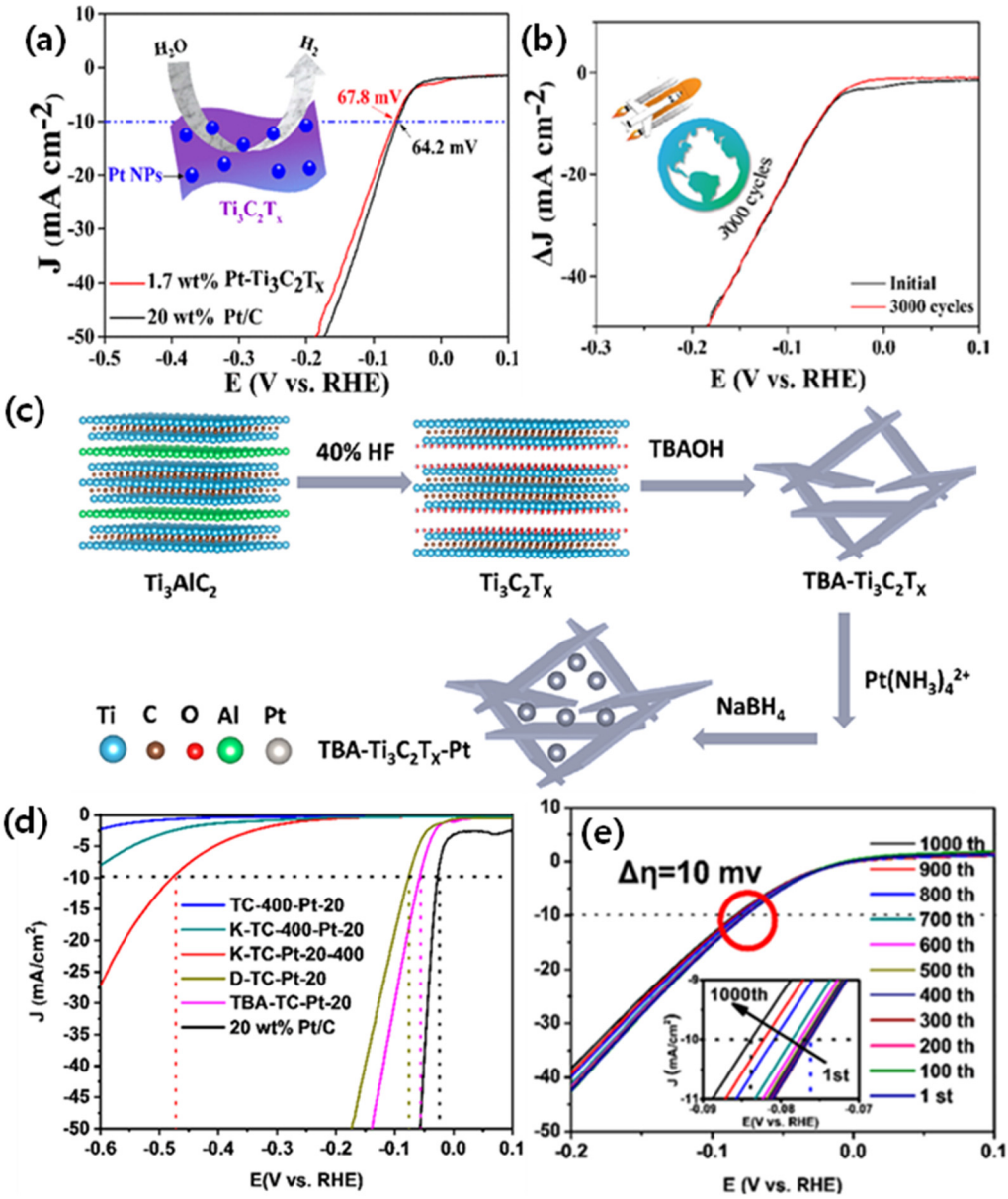

Figure 8. (**a**) Linear sweep voltammetry curves (**b**) Plotting of current—density difference (ΔJ) against the voltage scan rate of 1.7 wt% Pt-$Ti_3C_2T_x$ initial and 3000th cycle. (Reprinted with permission from Ref. [54]. Copyright 2020, American Chemical Society). (**c**) Schematics of the preparation process of TBA$Ti_3C_2T_x$-Pt. (**d**) Polarization curves of Pt deposited on the supports in 0.5 M H_2SO_4. (**e**) Polarization curves of TBA-$Ti_3C_2T_x$-20 obtained for 1000 cycles (Reprinted with permission from Ref. [81]. Copyright 2019, American Chemical Society).

In another study by Yuan et al. [81], the Pt nanoparticles are supported on the $Ti_3C_2T_x$ catalyst by a simple reduction in metallic precursors by a web impregnation method ($NaBH_4$ reduction method), and the Pt-deposited $Ti_3C_2T_x$ catalyst is then studied for HER reaction (Figure 8c). Various samples were synthesized, such as K-intercalated, tetrabutylammonium hydroxide (TBA) and the heat-treated (@400 °C) samples. Among all the samples, the TBA-TC-Pt-20 (corresponding to 1 wt% of the Pt) samples showed the best HER activity, whereas the heat-treated samples @ 400 °C showed the worst activity due to

the partial damage to the Ti−C layers of the supports. XPS analysis revealed that the Pt4f peaks are shifted to higher binding energies, indicating the strong interaction between Pt and the $Ti_3C_2T_x$ support, which in turn helps in the fast charge transfer burning the HER. The TBA-TC-Pt-20 catalyst showed a η of 55 mV, much higher than the other Pt catalysts. In addition, the TBA-TC-Pt-20 catalyst also showed admirable durability, with just 10 mV of the potential decrease after 1000 cycles (Figure 8d,e).

In a similar attempt to reduce the Pt loading, Wu et al. [82] developed a spray drying route to synthesize 3D crumbled $Ti_3C_2T_x$ supported with the atomic Pt clusters as highly active HER catalysts. The spray drying technique could avoid the successful re-stacking of $Ti_3C_2T_x$ and mitigate the agglomeration of the $Ti_3C_2T_x$ nanosheets during the catalyst deposition process, thereby increasing the exposure of the electrochemical active surface area. The colloidal tetrabutylammonium hydroxide intercalated $Ti_3C_2T_x$ nanosheets are mixed with the chloroplatinic acid solution, and the mixture is spray dried. Due to the presence of low-valance Ti^{2+}/Ti^{3+}, spontaneous reductions in the Pt^{4+} ions into Pt single atom/cluster are deposited on the $Ti_3C_2T_x$ nanosheets. SEM and TEM images clearly showed the 3D crumpled $Ti_3C_2T_x$ structure, on which the Pt clusters with homogeneous distribution were noticed. The Pt/ $Ti_3C_2T_x$ MXene catalyst showed extraordinary HER activity, with nearly zero onset potential and a η of 34 mV @ 10 mA cm^{-2}, nearly equal to Pt/C (37 mV). Further, the Pt loading of 2.9 wt% was achieved by the spray drying technique. When the HER activity is normalized by the mass, the Pt/MXene catalyst exhibits seven times over Pt/C. This is due to the high surface area of $Ti_3C_2T_x$ and the subatomic/clusters of Pt, which can expose more Pt surface area for HER than typical Pt nanoparticles on carbon support. Such a high HER mass activity was also supported by the DFT calculations. The PDOS analysis revealed that the d-band center shifted nearer to the ideal fermi level, indicating that the Pt on TiCO-F offered optimized binding energy for hydrogen atoms, which was neither too strong/too weak for the chemical reaction. In addition, ΔG_H* for Pt/TiCO-F was lower than the Pt (111), i.e., 0.05 eV vs. −0.18 eV. The shift in the d-band center and lower ΔG_H* for Pt/TiCO-F demonstrated the high HER activity of it.

6.2.5. Non-Pt/$Ti_3C_2T_x$-Based MXenes for HER

Among the non-Pt-based catalysts, the transition metal-based sulfides, phosphides, nitrides and carbides have attracted attention recently due to a variety of electrochemical reactions, including HER. Especially when hybridizing the transition metal derivatives with the support materials, such as carbon and 2D materials, e.g., carbon nanotubes, graphene, etc., it is found that the support materials offer essential surface area and electronic conductivity, which together expose the catalytic active sites [83]. In this regard, a variety of transition metal derivatives are hybridized with MXenes and are explored as efficient electrocatalysts in efforts to reduce the Pt catalyst price. Lu et al. [84] synthesized a $Co_2P/N@Ti_3C_2T_x$ supported on nickel foam (CPN@TC) as an ultra-efficient HER catalyst. The $Co_2P/N@Ti_3C_2T_x$ with the industrial potential is synthesized by an electrodeposition method on Ni foam as the substrate. The SEM images show the Ni foam is covered by the nanosheets of $Ti_3C_2T_x$. When the electrode potential is applied, the Co_2P nanoparticles are grown in the $Ti_3C_2T_x$ nanosheets ($Co^{2+} + 2e^- \rightarrow Co$, $2Co + H_2PO^{2-} + 2H^+ + e^- \rightarrow Co_2P + 2H_2O$). Further, the Co_2P nanostructures are then converted into nitrides by the process of nitridation by using ammonium carbonate decomposition. Nitridation is known to increase conductivity, and hence, it results in a better electrocatalytic activity. Nitridation also replaces some of the surface functional groups, such as -F, -O and -OH, together with the doping of N into the Co_2P to form N-doped Co_2P. Such multi-heterojunction interfaces in the $Co_2P/N@Ti_3C_2T_x$ could offer unique 3D interfacial electron transfer pathways for improved HER activity. The resulting $Co_2P/N@Ti_3C_2T_x$ showed extraordinary HER activity with a η of 15 mV @−10 $mAcm^{-2}$ and a Tafel slope close to 30 mV dec^{-1}. In terms of durability, the $Co_2P/N@Ti_3C_2T_x$ catalyst showed no obvious change in potential for 60 h of operation at −10 $mAcm^{-2}$, and under potential cycling conditions, it

showed a marginal loss of just 2 mV after 3000 cycles, indicating the potentiality of this catalyst in industrial applications (Figure 9). In another study, Han et al. [85] synthesized multi-dimensional hierarchical CoS_2@MXene through a hydrothermal reaction followed by the sulfurization process. Nanowires of CoS_2 were attached to $Ti_3C_2T_x$ with no obvious agglomerations. XPS analysis showed the Co and S peaks shifted to a high binding energy when hybridized with $Ti_3C_2T_x$, indicating the strong interaction between CoS_2 and $Ti_3C_2T_x$. However, the CoS_2@MXene catalyst still showed a large overpotential of 175 mV@10 mAcm^{-2}. Jiang et al. [86] synthesized transition metal-based chalcogenide core shell nanostructure Ti_3CNCl_2@CoS_2 as an excellent HER catalyst. The Cl-terminated MXenes were synthesized by the molten salt method, and the CoS_2 nanostructures were deposited by a hydrothermal synthesis process. Through a DFT analysis, the hybridization of CoS_2 with Ti_3CNCl_2 effectively brought down the ΔG_H* to −0.1 eV from their individual constituents of −0.89 and +1.86 eV, respectively. SEM images and elemental mapping indicated that the Ti, N, Cl were present at the center, whereas the Co and S elements were seen on the peripheral part of the core shell nanoparticles. With the optimized 7.63% of CoS_2, the Ti_3CNCl_2@CoS_2 catalyst showed improved HER activity compared to its constituent CoS_2 with Ti_3CNCl_2.

Another transition metal, Ni, and its derivatives, such as NiP and $NiSe_2$, have also attracted a lot of attention due to the fact that Ni derivatives are chemically stable and accelerate the HER kinetics [87]. Lu et al. [88] synthesized NiP/$Ti_3C_2T_x$ supported by a 3D Ni foam by a hydrothermal method, followed by phosphorylation. The ultraviolet photoelectron spectroscopy (UPS) was used to understand the band structure and work function. It was observed that the valance band maximum (E_v) of the NiP/$Ti_3C_2T_x$ catalyst showed a larger value than $Ti_3C_2T_x$. In addition, the work function of NiP/$Ti_3C_2T_x$ was found to be lower (2.13 eV) than $Ti_3C_2T_x$ (2.2 eV). Both the E_v and work function proved that the electrons in the NiP/$Ti_3C_2T_x$ are more easily accessible for electrochemical reactions. The NiP/$Ti_3C_2T_x$ catalyst showed a η of 135 mV @10 mA cm^{-2}. Through a DFT analysis, the ΔG_H* of NiP/$Ti_3C_2T_x$ was found to be −0.28 eV, close to that of ΔG_H* of Pt (−0.09 eV). In another study, Jiang et al. [89] synthesized octahedral $NiSe_2$-supported $Ti_3C_2T_x$ by a one-pot hydrothermal synthesis. The $Ti_3C_2T_x$ nanosheets were mixed with the $NiCl_2$-EDTA and the Se (KOH) solution, which forms the Ni-EDTA chelated complex, which, upon the hydrothermal conditions, forms the octahedra $NiSe_2$ supported by MXenes. HRTEM images show the perfect single-crystal nature of $NiSe_2$ with a d spacing of 0.27 nm corresponding to a (210) plane and 1.0 nm of $Ti_3C_2T_x$ corresponding to a (002) plane. The strong coupling interaction between the $Ti_3C_2T_x$ and $NiSe_2$ is further established by the XPS analysis in which the Ni2p peaks shift to a higher binding energy by 0.3 and 0.6 eV Ni $2p_{3/2}$ and Ni $2p_{1/2}$, respectively. Nevertheless, $NiSe_2$/$Ti_3C_2T_x$ showed a large overpotential (200 mV @10 mA cm^{-2}) when compared to all the other types of catalysts discussed in the earlier sections, indicating that selenides might have a lower HER activity over sulphides, phosphides and nitrides.

Guided by the DFT calculations, the doping of Nb with $Ti_3C_2T_x$ modified the electronic conductivity of the support by lifting the fermi level, and, at the same time, alloying Ni and Co efficiently adjusted the M-H attraction, synergistically enhancing the HER activity (Du et al. [90]). The ΔG_H* of the Ti_3C_2 and Nb-doped Ti_3C_2 catalysts is found to be −0.25 eV and −0.14 (O site nearby Nb-doped atoms) and −0.23 eV (O site nearby Nb-doped atoms), indicating that Nd-doped Ti_3C_2 could deliver enhanced HER activity. Further, by adding Co and Ni atoms, the ΔG_H* values further decreased to more than half of the Nb-doped Ti_3C_2 catalyst. HR-TEM images show the multilayered, crumbled nanosheet morphology of $Ti_{2.5}Nb_{0.5}C_2T_x$ and $Ni_{0.9}Co_{0.1}$ alloy nanoparticles of 5 nm are deposited. Electrocatalytic HER of the NiCo@NTM is evaluated in 1 M KOH. The IR corrected NiCo@NTM LSV curves show a η of 43.4 mV @ 10 mA cm^{-2}, which is almost close to the benchmark Pt/C (34.4 mV). Further, when the current densities are normalized by the double layer capacitance (C_{dl}) J_{cdl} @ 1000 mA F^{-1}, the NiCo@NTM catalyst exhibits a lower overpotential of 55.5 mV, higher than the Pt/C. Impedance spectroscopy also suggests a lower resistance to the NiCo@NTM

catalyst. During the stability test, the NiCo@NTM catalyst also showed excellent durability over 50 h in the chronopotentiometry test. Therefore, it is reasonable that the NiCo@NTM catalyst is a promising non-precious-metal catalyst for HER in alkaline medium.

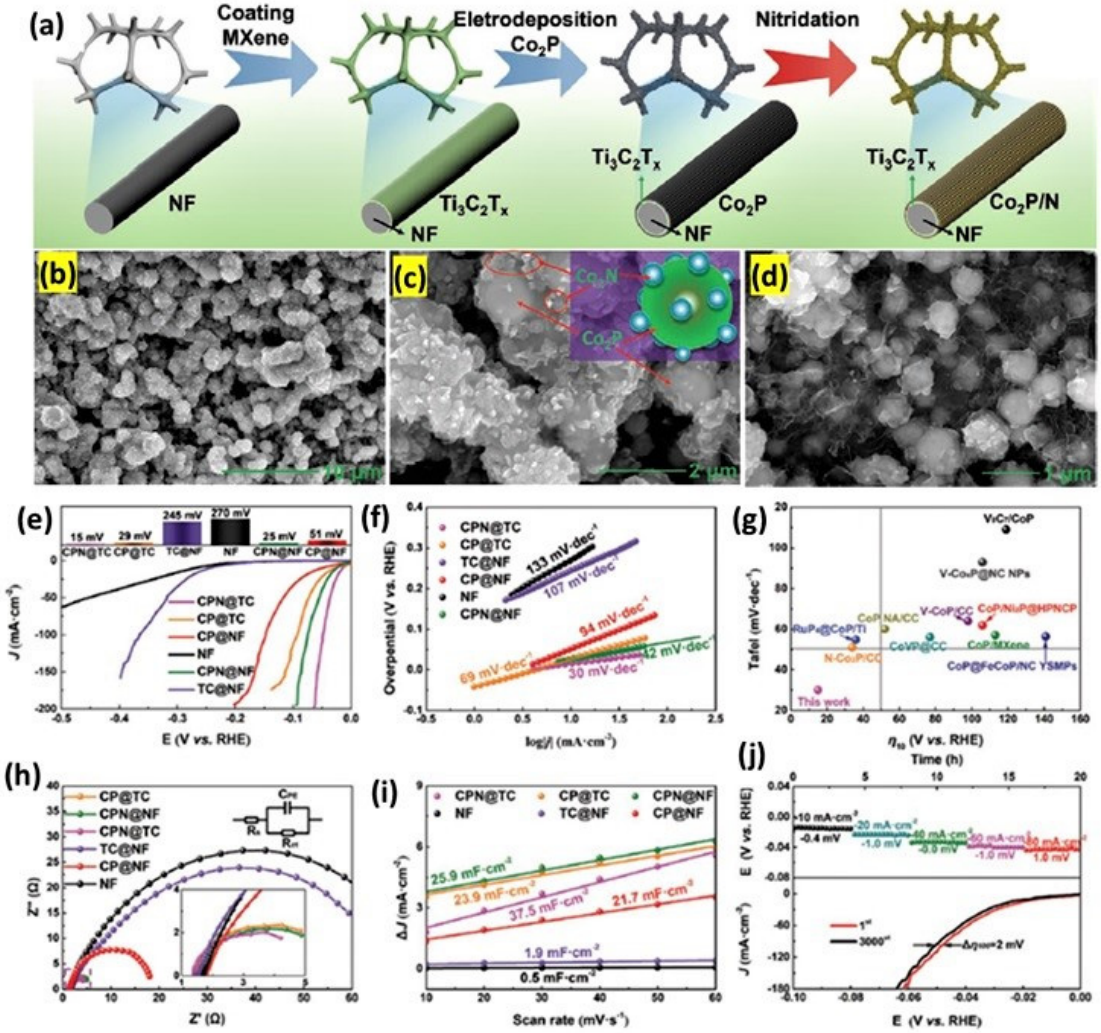

Figure 9. (**a**) Schematic illustration of the catalyst synthesis strategy. (**b**–**d**) SEM images of (**b**–**d**) CPN@TC. (**e**) Polarization curves and (**f**) corresponding Tafel slopes of CPN@TC, CP@TC, CP@NF, NF, CPN@NF and TC@NF. (**g**) Comparison of CPN@TC with reported electrocatalysts. (**h**) EIS patterns and (**i**) the C_{dl} of CPN@TC, CP@TC, CP@NF, NF, CPN@ NF and TC@NF. (**j**) Long-term chronopotentiometry response of CPN@TC at different current densities (−10, −20, −40, −60, −80 mA cm^{-2}) and polarization curves for CPN@TC before and after 3000 cycles (Reprinted with permission from Ref. [84]. Copyright 2021, John Wiley and Sons).

6.2.6. Nb_2CT_x-Based MXenes for HER

It is considered that the research on MXenes is in its infancy. Theoretical simulations suggest more than 70 types of MXenes are possible; however, until now, very few MXenes have been successfully synthesized and explored for electrochemical reactions. Among them, $Ti_3C_2T_x$ has been the most explored MXene. However, recently, there have been other types of MXenes also gaining special attention. For example, Tan et al. [91] investigated the HER performance of pristine $Nb_4C_3T_x$ in acidic and alkaline electrolytes. Similar to $Ti_3C_2T_x$, the $Nb_4C_3T_x$ MXene was synthesized from Nb_4AlC_3 by HF etching. The SEM images show that the compact Nb_4AlC_3 structure is loosened and exhibit the layered structure in $Nb_4C_3T_x$, indicating the successful etching of the Al layer. The etching process was carried out at room temperature at different times in the HF solution, which was varied

between 140 h to 220 h. An optimum time of 180 h was found suitable for sufficiently removing the Al layer, analyzed by calculating the ratio of I_{MAX}/I_{MXene} (I_{MAX} and I_{Mxene} represents the diffraction peak intensity of (103) for Nb_4AlC_3 and (002) for $Nb_4C_3T_x$, respectively). The $Nb_4C_3T_x$-180 sample showed the lowest I_{MAX}/I_{Mxene}, which indicated that the Al layer was removed by stirring for 180 h. When comparing the HER activity of all the $Nb_4C_3T_x$ treated at different time intervals, $Nb_4C_3T_x$-180 showed better HER activity (398 mV @ 10 mA cm^{-2}) than the other catalysts. However, the $Nb_4C_3T_x$-180 HER activity was far behind the Pt/C catalyst. However, when the Pt nanoparticles were introduced to $Nb_4C_3T_x$, the HER activity was enhanced by several-fold (Figure 10a,b).

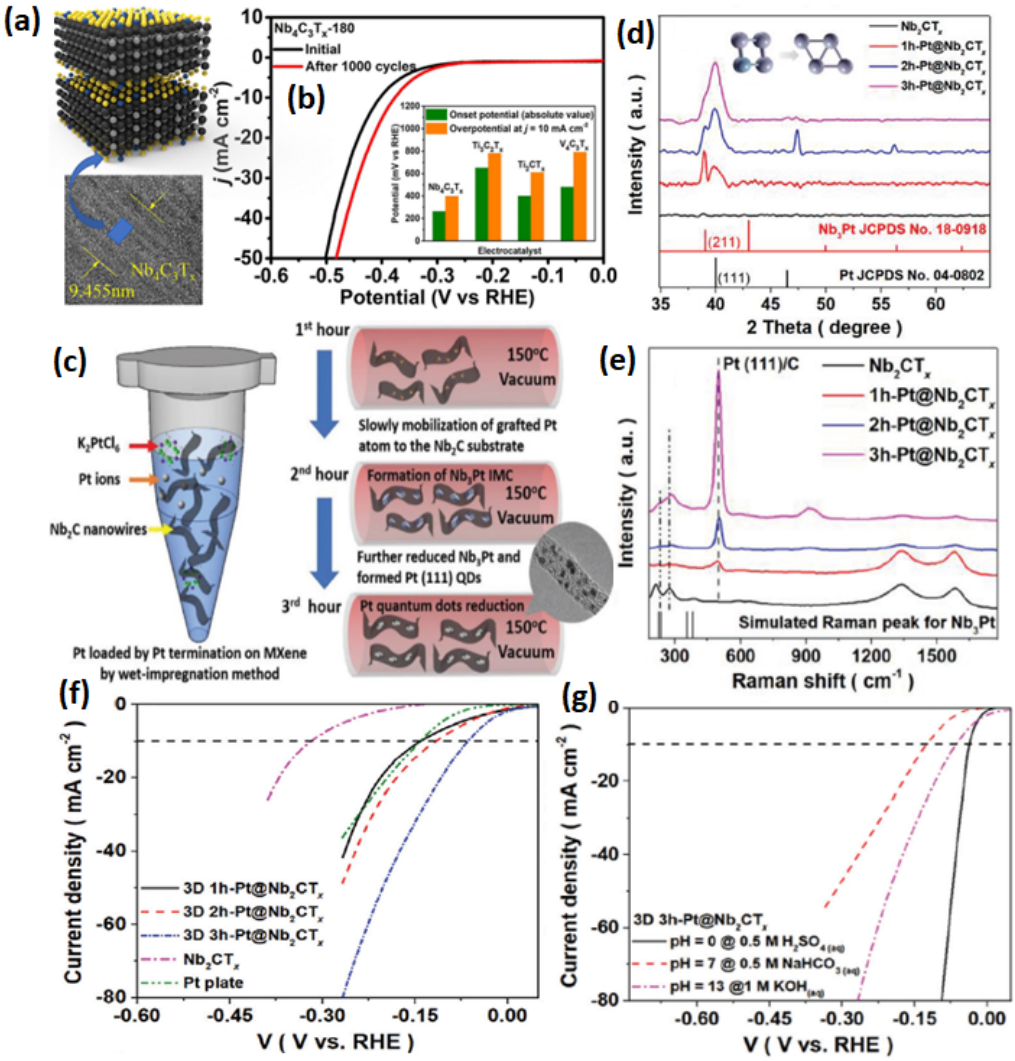

Figure 10. (**a**) Schematic of Nb4C3Tx. (**b**) Polarization curves of the Nb4C3Tx-180 electrode before and after 1000 cycles at 100 mV s^{-1} under an alkaline onset potential and overpotential at j @ 10 mA cm^{-2} in different MXenes conditions (Reprinted with permission from Ref. [91]. Copyright 2021, Elsevier) (**c**) Schematic for the fabrication of Pt QDs on Nb2CTx NWs. (**b**,**c**) Structural investigation of various Pt QDs on MXene by their (**d**) XRD patterns and (**e**) Raman spectra. (**f**) LSV for 3D Pt@Nb2CTx with different synthesis times (**g**) The LSV for 3D 3h-Pt@Nb_2CTx in different electrolytes (Adapted from Ref. [92], Open access).

Pang et al. [92] reported the nanowire morphology of 1D Nb_2CT_x as a HER catalyst. The nanowire morphology of 1D Nb_2CT_x was obtained by the electrochemical etching process. The 1D Nb_2CT_x has a length of 100–400 nm and a width of 50 nm. The Pt is impregnated onto 1D Nb_2CT_x by a process of wet impregnation, with Pt nanoparticle size of 2 nm. The resulting Pt@Nb_2CT_x exhibited an overpotential of 33.3 mV in acidic

and 65.1 mV in basic electrolytes @ 10 mA cm^{-2}. The high HER activity was attributed to the strong metal support interaction between Pt and Nb_2CT_x, evidenced structurally, morphologically and through spectroscopic methods. The strong interaction also offers robustness and stability (Figure 10c–g). In another study, Fan et al. [93] mechanochemically synthesized Pt/Nb_2CT_x and obtained excellent HER activity, close to the commercial Pt/C catalyst. Typically, the Nb_2CT_x powder was mixed with the solution of $PtCl_6^{2-}$ and ball milled at the speed of 150 rpm for about 30 min. Then, the power was subjected to annealing at 600 °C for 2 h under the Ar gas. The TEM images show the nanoclusters of Pt were introduced on the Nb_2CT_x of about 1.5 nm. During the annealing process, the Pt also alloyed with Nb to five Pt_3Nb nanoparticles. The HER analysis shows that the Pt/Nb_2CT_x-600 catalyst showed excellent activity compared to the Pt/Nb_2CT_x and Pt/C catalysts. At the current density of 10 mA cm^{-2}, the Pt/Nb_2CT_x-600 catalyst exhibited a η of 5 mV, lower than the 6.2 mV for Pt/C. In addition, the Pt/Nb_2CT_x-600 catalyst also exhibited excellent durability, with no loss in η after 5000 cycles and a marginal loss in the relative current after 20 h. The excellent HER activity of the Pt/Nb_2CT_x-600 catalyst is attributed to the strong metal support interaction and homogeneous distribution of Pt and Pt_3Nb nanoparticles on the Nb_2CT_x support.

6.2.7. $V_4C_3T_x$-Based MXenes for HER

A new class of $V_4C_3T_x$ MXenes has gained special interest in recent years due to its applications in lithium-ion batteries, as a positive electrode in sodium ion capacitors and as an electrocatalyst for CO_2 capture [94]. However, for HER, it has been very rarely investigated. Ling et al. [95] predicted that highly catalytically active V_2CO_2 MXene supported Fe, Co and Ni for HER catalysis. As it is known that a synthesis of any type of MXenes needs to have obvious oxygen functionalities, therefore, the modeling was performed with oxygen terminations. When H adsorbs on V_2CO_2, the H 1s orbital and terminated O $2p_z$ orbital hybridize to form the bonding orbital and the antibonding orbital (σ and σ*). When the σ* occupancy is higher, the bonding strength of H will be higher. By introducing the metal atoms, which act as metal donors, a higher electron transfer occurs from metal atoms to -O, and thereby, there is a higher occupancy in the σ* that leads to O-H bonding. The higher charge on the O atom due to electron transfer from the metal center leads to decreased charge transfer from H to O; therefore, the interaction between O and H will be weakened. This promotes the optimal adsorption for HER kinetics (Figure 11a,b). When the transition metal (TM) supported V_2CO_3, the binding energies (E_b) were observed to be higher than 1.0 eV, indicating a strong interaction between V_2CO_3 and TM. Among all the investigated TM, a significant promotional effect (0.7 e^- from TM to V_2CO_2) is observed for Fe, Co and Ni, and the calculated ΔG_H is from Fe to Co to Ni-V_2CO_2; therefore, it is concluded that the HER activity of Fe-V_2CO_2 is to be higher than the other TM-V_2CO_2 catalysts. Not many experimental studies are found to investigate the Vanadium-based MXenes. Tran et al. [96] investigated the HER activity of pristine $V_4C_3T_x$. It is seen that the pristine $V_4C_3T_x$ showed a η of 200 mV @ 10 mA cm^{-2}. Park et al. [97] reported the atomic Pt deposited V_2CT_x. It is believed that HF etching creates the V vacancies, which act as metal immobilizing sites for Pt deposition (Figure 11c). A loading as low as ~0.88 wt% and the identification of Pt-C bonding are responsible for the excellent, Pt-like HER activity of the Pt/V_2CT_x catalyst. The V vacancies that are naturally formed during the Al etching process are known to be highly unstable and reductive in nature. When $PtCl_6^{2-}$ ions are added to the exfoliated V_2CT_x, the $PtCl_6^{2-}$ are spontaneously adsorbed on the V vaccines and are reduced by the reductive nature of V vaccines to metallic Pt. The atomic distribution of the Pt atoms is revealed by the HAADF-STEM analysis in which the Pt atomic sites are seen with bright spots on the V_2CT_x nanosheets. Further, it is seen that the Pt atoms are located at the V lattice plane, evidencing that V vacancies attract and stabilize the Pt atoms. The HER analysis reveals that the Pt-V_2CT_x catalyst showed higher activity (27 mV of η @ 10 mA cm^{-2}) than the Pt/C (36.5 mV of η @ 10 mA cm^{-2}). While the Pt loading on V_2CT_x is ~19 times (~0.88 wt%) lower than the commercial Pt/C (20 wt%), when

normalizing the HER mass activity, extraordinarily, the Pt-V_2CT_x catalyst was 50 times higher (7.88 A mg_{pt}^{-1} @ η of −30 mV) than the commercial Pt/C catalyst (0.157 A mg_{pt}^{-1} @ η of −30 mV). Similar statistics were also drawn, in turn, over the frequency analysis, in which the Pt-V_2CT_x showed a TOF of 4.74 and 1.16 H_2 S^{-1}, whereas for Pt/C, it was 0.156 and 0.0226 H_2 S^{-1} (Figure 11d–i). The HER activity obtained in this study is one of the best among several other types of MXenes, even higher than the P-doped V_2CT_x [98].

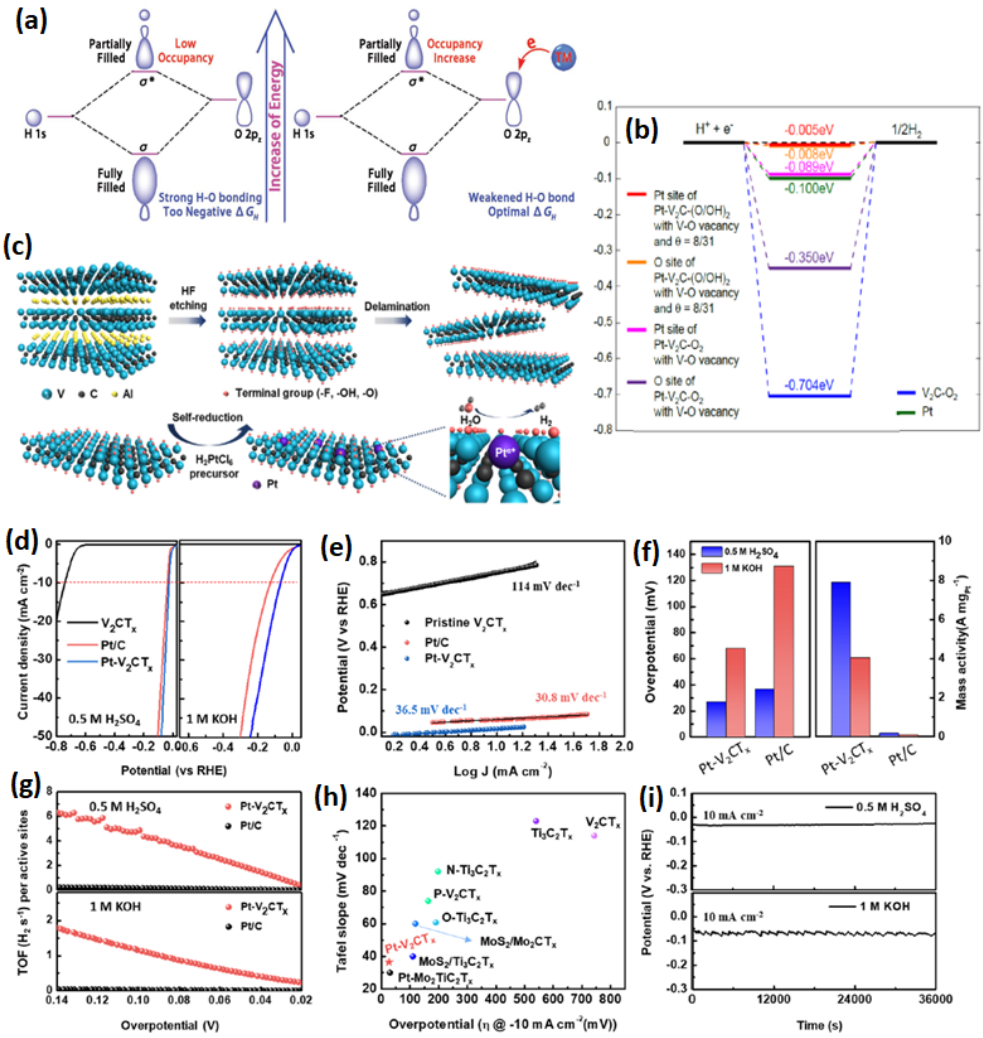

Figure 11. The scheme of modulating the HER performance of V_2CO_2 by introducing transition metal onto the surface. (**a**) The combination of H 1s orbital and O 2pz orbital forms a fully filled bonding orbital and a partially filled anti-bonding orbital, in which the occupancy of anti-bonding orbital will determine the strength of H O bond. (**b**) Structural characteristics of Pt-V_2CT_x nanosheets (Adapted from Ref. [95] Open access). (**c**) Schematic illustration for synthesis of Pt-V_2CT_x nanosheets. Electrocatalytic performance for Pt-V_2CT_x and reference HER electrocatalysts. (**d**) HER polarization curves of pristine V_2CT_x, Pt/C (20%) and Pt-V_2CT_x, acquired using graphite rod as the counter electrode in 0.5 M H_2SO_4 solution (left) and in 1 M KOH solution (right). (**e**) Corresponding Tafel slope derived from a. (**f**) Comparison of overpotential (10 mA cm^{-2}) and mass activity for Pt/C (20%) and Pt-V_2CT_x catalysts in 0.5 M H_2SO_4 (blue) and 1 M KOH (red). (**g**) Turnover frequency (TOF) of Pt/C (20%) and Pt-V_2CT_x in 0.5 M H_2SO_4 solution (top) and in 1 M KOH solution (bottom). (**h**) Comparative graph for overpotential of related MXene-based HER electrocatalysts in acidic media. (**i**) Stability test of Pt-V_2CT_x in 0.5 M H_2SO_4 solution (top) and 1 M KOH (bottom). (Reprinted with permission from Ref. [97]. Copyright 2021, Elsevier).

6.2.8. Mo_2CT_x-Based MXenes for HER

Among the other MXenes, the Mo-based MXenes are gaining particular interest due to the fact that the Mo-based-MAX phases can be easily converted into catalytically active 2D MoS_2. It is well known that, theoretically, 2D MoS_2 show ideal an ΔG_H, close to zero. Further synthesis of a solid solution or substitution of cobalt in Mo_2CT_x is found to be one of the effective ways to fine tune the Mo_2CT_x HER activity, especially in alkaline medium. DFT calculations also reveal that the substitution of Co significantly changes the thermodynamics and adsorption energies that favor enhanced HER activity [99]. Liu et al. [100] synthesized CoP-supported Mo_2CT_x for HER reaction. The NH_4F-etched Mo_2Ga_2C produced the layered Mo_2CT_x. Mo_2CT_x was negatively charged due to the surface terminations; the Co^{2+} ions were attracted electrostatically. The hydrothermal treatment and subsequent phosphorylation produced the CoP catalyst supported on Mo_2CT_x (CoP/Mo_2CT_x). The CoP/Mo_2CT_x showed a HER activity with an overpotential of 78 mV at a current density of 10 mA cm^{-2}. Figure 10a shows the LSV curves of CoP/$Mo_2CT_{x'}$, comparing its performance with CoP, Co(OH)F/Mo_2CT_x and Mo_2C precursor materials. It shows that CoP/Mo_2CTx had the lowest overpotential at all current densities. It signifies that the synergistic effect between CoP and Mo_2C MXene promoted the HER catalytic activity compared to the individual materials. Further, to check the reaction kinetics, the Tafel slopes were obtained from the LSV curves, as shown in Figure 12b,c. The obtained Tafel slope values for CoP/Mo_2CT_x, CoP, Co(OH)F/Mo_2CT_x and Mo_2C MXene were 66, 95, 158 and 192 mV dec^{-1}, respectively. Among them, CoP/Mo_2CT_x had the lowest Tafel slope, and it was close to the value of Pt/C (40 mV dec^{-1}), signifying the identical reaction pathway. The rate determining step was the desorption of H_2. To test the stability, the CoP/Mo_2CT_x electrode was kept at the current density of 10 mA cm^{-2} for 50 h and observed 89% retention of the initial current, as shown in Figure 12d–f.

Tan et al. [101] developed a mesh carbon-coated $MoSe_2$/Mo_2CT_x hybrid material ($MoSe_2$/Mo_2CT_x@C), which took an overpotential of 108.3 mV to reach 10 mA cm^{-2} current density in acidic medium (0.5 M H_2SO_4 solution). The LSV curves of the $MoSe_2$/Mo_2CT_x@C catalyst are shown along with the individual $MoSe_2$ (η = 296.3 mV) and Mo_2CT_x (η = 325.3 mV) catalysts; $MoSe_2$/Mo_2CT_x@C show good catalytic activity. The obtained Tafel slopes of $MoSe_2$/Mo_2CT_x@C, $MoSe_2$/Mo_2CT_x, $MoSe_2$ and Mo_2CT_x catalysts were found to be 70.7, 122.1, 108.7 and 152.1 mV dec^{-1}, respectively. Among them, $MoSe_2$/Mo_2CTx@C showed the lowest Tafel slope compared to the individual components, and its value showed that it performed the HER via the Volmer–Heyrovsky mechanism. The enhanced reaction kinetics was due to improved conductivity from $MoSe_2$, Mo_2CT_x and the carbon coating layer composite. The stability of the $MoSe_2$/Mo_2CT_x@C catalyst was evaluated using cyclic voltammogram and chronoamperometry techniques. In addition, after 1000 cycles, there was no considerable loss in the activity compared to the initial curve. The chronoamperometric curve of $MoSe_2$/Mo_2CT_x@C also showed a stable current density up to 24 h, indicating that the good structural stability of $MoSe_2$/Mo_2CT_x@C was durable. This could be due to the mixed $MoSe_2$/Mo_2CT_x@C composite. Lim et al. [102] reported Mo_2CT_x/2HMoS_2 nanohybrid catalytic activity in 0.5 M H_2SO_4 electrolyte. Due to the intimate epitaxial coupling at the Mo_2CT_x/2H-MoS_2 nanohybrid interface, it afforded superior HER activities, taking only 119 or 182 mV overpotential to reach −10 or −100 mA cm^{-2} current densities, respectively. It is observed that the Tafel slope of Mo_2CT_x/2HMoS_2 was 60 mV dec^{-1}, which was significantly lower compared to the bare untreated d Mo_2CT_x (91 mV dec^{-1}) and a physical mixture of d-Mo_2CT_x with 2H-MoS_2 NPs (85 mV dec^{-1}). Noticeably, the Mo_2CT_x/2H-MoS_2 nanohybrid's Tafel slope was maintained up to −450 mA cm^{-2}, unlike other metal catalysts, which exhibited increased Tafel slopes, and hence, steeply increasing overpotentials, at higher current densities. In addition, Mo_2CT_x/2HMoS_2 also exhibited excellent stability up to 10,000 cycles (Figure 12g–i).

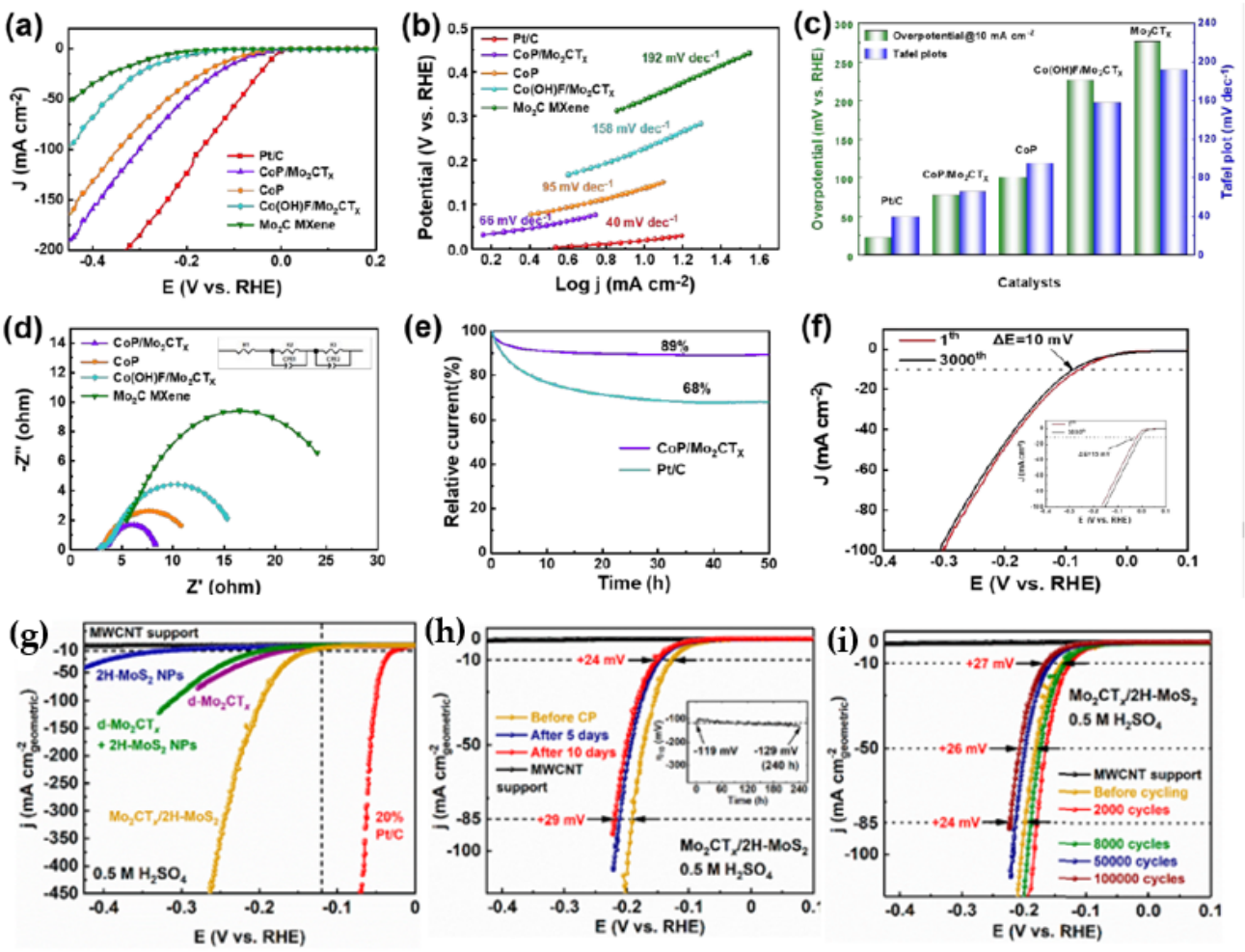

Figure 12. (**a**) LSV curves, (**b**) Tafel plots, (**c**) The Tafel slope and overpotential @10 mA cm^{-2} for Pt/C, CoP/Mo_2CT_x, CoP, Co(OH)F/Mo_2CT_x, Mo_2C MXene in 1 M KOH. (**d**) The electrochemical impedance spectra (EIS), (**e**) Chronoamperometric curves of CoP/Mo_2CT_x and Pt/C at the current density of 10 mA cm^{-2} for 50 h. (**f**) LSV curves of CoP/Mo_2CT_x catalyst before and after 3000 CV cycles, and inset is the corresponding LSV curves before and after 3000 CV cycles for Pt/C. Reprinted with permission from Ref. [100]. Copyright 2021, Royal Society of Chemistry. (**g**) iR-corrected CV polarization curves for Mo_2CT_x/2H-MoS_2 nanohybrid in 0.5 M H_2SO_4 after (**h**) 10-day CP (constant current at −10 mA cm^{-2}_{geom}, inset shows time-dependent iR-corrected overpotential during CP) and (**i**) 100,000 accelerated CV cycling at 100 mV s^{-1}. HER electrochemical stability results of (Reprinted with permission from Ref. [102] Copyright 2020 American Chemical Society).

Ren et al. [103] reported 2D organ-like molybdenum carbide (MXene) coupled with MoS_2 (MoS_2@Mo_2CT_x) nanoflowers. The LSV curves of MoS_2@Mo_2CT_x were recorded in aqueous 1.0 M KOH solution along with Mo_2Ga_2C, Mo_2CT_x, MoS_2 and Pt/C for comparison purpose. The observed overpotential of MoS_2@Mo_2CT_x was 176 mV at a current density (j) of 10 mA cm^{-2}, which was less compared to the values of Mo_2Ga_2C (897 mV), Mo_2CT_x (533 mV) and MoS_2 (394 mV) electrocatalysts. The Tafel slopes of the corresponding as-prepared catalysts were calculated to be 308, 208, 186, 207 and 98 mV dec^{-1} for Mo_2Ga_2C, MoS_2, Mo_2CT_x, MoS_2@Mo_2CT_x and Pt/C, respectively. The smaller Tafel slope of MoS_2@Mo_2CT_x indicated that the HER may follow the Volmer–Heyrovsky mechanism. The obtained results show that MoS_2@Mo_2CT_x had a good electrocatalytic activity toward HER, which was due to a greater number of active sites and good electrical conductivity. For useful information to the readers, we summarized the HER performance of MXene catalysts [89,104–142] in Table 2. In addition, to compare the status of MXene-based catalysts

with the other 2D materials, the HER performances of the catalysts are given in Table 3. After analyzing the HER performance, it was observed that the activities of pristine MXenes were much lower than the other 2D materials. However, the Pt and non-Pt deposited MXenes showed comparable HER performances to other 2D materials, such as graphene, TMDs, LDHs and g-C_3N_4-based catalysts, and in some cases, better HER performance. Figure 13 shows the benchmark figures of the Mxene catalysts with respect to commercial Pt/C. The benchmark Figure 13 shows that several MXene-based catalysts showed nearing performance with Pt/C, and some Pt-supported $Ti_3C_2T_x$ showed an even lower overpotential than Pt/C (indicated by green color in Figure 13). This comparison clearly indicates that with further improvements, MXenes-based catalysts could be potential HER catalyst alternative to traditional Pt/C-based catalysts.

Table 2. Summary of electrochemical performance of MXene-supported catalysts for HER.

Catalyst	Overpotential (mV) @ 10 mA cm^2	Electrolyte	Ref
Pristine/Functionalized/Heteroatom-doped MXenes			
Mo_2CT_x	189	0.5 M H_2SO_4	[104]
$Ti_3C_2T_x$	538	0.5 M H_2SO_4	[105]
F-Ti_2CT_x	170	0.5 M H_2SO_4	[75]
O-$Ti_3C_2T_x$	190	0.5 M H_2SO_4	[106]
$V_4C_3T_x$	200	0.5 M H_2SO_4	[96]
Nb_4C_3T	398	1.0 M KOH	[91]
$Ti_3C_2T_x$ nanofibers	169	0.5 M H_2SO_4	[107]
VOOH/$Ti_3C_2T_x$	100	1.0 M KOH	[108]
N-$Ti_3C_2T_x$	215	0.5 M H_2SO_4	[77]
N-$Ti_3C_2T_x$@600	198	0.5 M H_2SO_4	[78]
P-Mo_2CT_x	114	0.5 M H_2SO_4	[109]
N-$Ti_3C_2T_x$-35	162	0.5 M H_2SO_4	[79]
P-V_2CT_x	220	0.5 M H_2SO_4	[102]
P-TiO_2@Ti_3C_2	97	1.0 M KOH	[110]
Pt/$Ti_3C_2T_x$-based catalysts			
Pt/C	29	0.5 M H_2SO_4	[102]
Pt/$Ti_3C_2T_{x\text{-}550}$	32.7	1.0 M $HClO_4$	[111]
TBA-$Ti_3C_2T_x$-Pt-20	70	0.5 M H_2SO_4	[81]
TBA-$Ti_3C_2T_x$-Pt	55	0.5 M H_2SO_4	[81]
PtNPs/$Ti_3C_2T_x$	226	0.1 M H_2SO_4	[112]
$Pt_{3.21}Ni$@Ti_3C_2	18.55	0.5 M H_2SO_4	[106]
$Pt_{3.21}Ni$@Ti_3C_2	55.6	0.1 M KOH	[113]
$Ti_3C_2T_x$@Pt/SWCNTs	62	0.5 M H_2SO_4	[114]
Pt NCs-MXene	40	0.5 M H_2SO_4	[115]
40Pt-TBA-$Ti_3C_2T_x$	67.8	0.5 M H_2SO_4	[80]
$Ti_3C_2T_x$@0.1Pt	43	0.5 M H_2SO_4	[116]
PtO_aPdO_bNPs@$Ti_3C_2T_x$	26.5	0.5 M H_2SO_4	[117]
$Mo_2TiC_2T_x$-Pt_{SA}	30	0.5 M H_2SO_4	[118]
Ru_{SA}-N-S-$Ti_3C_2T_x$	76	0.5 M H_2SO_4	[119]
Ru@B-$Ti_3C_2T_x$	62.9	0.5 M H_2SO_4	[120]

Table 2. *Cont.*

Catalyst	Overpotential (mV) @ 10 mA cm^2	Electrolyte	Ref
Non-Pt/$Ti_3C_2T_x$-based catalysts			
$Ni_{0.9}Co_{0.1}$@Nb-$Ti_3C_2T_x$	43.4	1.0 M KOH	[90]
Co^{3+}-Ti_2CT_x	458	1.0 M KOH	[121]
$Ni_{0.9}Fe_{0.1}PS_3$@ $Ti_3C_2T_x$	196	1.0 M KOH	[122]
MoS_2/Ti_3C_2-MXene@C	135	0.5 M H_2SO_4	[123]
MoS_2/$Ti_3C_2T_x$ nanoroll	168	0.5 M H_2SO_4	[124]
CoP@3D $Ti_3C_2T_x$	168	1.0 M KOH	[125]
$MoSe_2$/$Ti_3C_2T_x$	95	1 M KOH	[126]
$Co_xMo_{2-x}C$/MXene/NC	75	1.0 M KOH	[127]
$Co_xMo_{2-x}C$/MXene/NC	81	0.5 M H_2SO_4	[127]
Mo_2C/$Ti_3C_2T_x$@NC	53	0.5 M H_2SO_4	[128]
Mo_2C/$Ti_3C_2T_x$@NC	75	1.0 M KOH	[128]
NiFe-LDH/$Ti_3C_2T_x$	132	1.0 M KOH	[129]
NiFe-LDH/MXene/NF	205	1.0 M KOH	[129]
P-Mo_2C/Ti_3C_2@NC	177	0.5 M H_2SO_4	[130]
CoP/Ti_3C_2	71	0.5 M H_2SO_4	[131]
CoP/Ti_3C_2 MXene	102	1.0 M KOH	[131]
$TiOF_2$@$Ti_3C_2T_x$	103	0.5 M H_2SO_4	[132]
$Co_{0.31}Mo_{1.69}C$/MXene/NC	75	1.0 M KOH	[133]
Ag@N-$Ti_3C_2T_x$	153	1.0 M KOH	[134]
3D CNTs@$Ti_3C_2T_x$	93	1.0 M KOH	[135]
$NiSe_2$/$Ti_3C_2T_x$	200	2.0 M KOH	[89]
Co-CoO/Ti_3C_2-MXene	45	1.0 M KOH	[136]
MoS_2@Ti_3C_2	110	0.5 M H_2SO_4	[137]
MoS_2-Ti_3C_2	98	0.5 M H_2SO_4	[138]
$NiFe_2O_4$/Ti_3C_2	173	0.5 M KOH	[139]
Nb_2CT_x/ $V_4C_3T_x$/ Mo_2CT_x-based catalysts			
Pd/Nb_2C-HF	34	0.5 M H_2SO_4	[76]
Co^{3+}-V_2CT_x	460	1.0 M KOH	[122]
NiS_2/V_2CT_x	179	1 M KOH	[140]
Co-MoS_2@Mo_2CT_x	112	1.0 M KOH	[141]
Mo_2CT_x:Co	180	1 N H_2SO_4	[99]
MoS_2@Mo_2CT_x	176	1.0 M KOH	[103]
MoS_2CT_x/2H-MoS_2	119	0.5 M H_2SO_4	[102]
MD-Ti_3C_2/MoS_x-100	165	0.5 M H_2SO_4	[142]
$NiSe_2$/$Ti_3C_2T_x$	200	0.5 M H_2SO_4	[89]

Table 3. Comparison of MXenes HER performance with the other 2D-layered non-precious-based electrocatalysts in acidic and alkaline media.

2D Material	2D Materials-Based Catalysts	Electrolyte	Overpotential (mV) at 10 mA cm^{-2}	Ref
Graphene	MoS_2@pr-GO	0.5 M H_2SO_4	263	[143]
	P-doped WN/r-GO	0.5 M H_2SO_4	85	[144]
	NG@Co@Zn@NF-850	1 M KOH	34	[145]
	Ni_3S_2@NGCLs/NF	1 M KOH	134	[146]
	Porous $MoSe_2$ Nanosheets	0.5 M H_2SO_4	150	[147]
	$ReSe_2$ nanoflakes/rGO	0.5 M H_2SO_4	145	[148]
	$Ni_{0.85}Se$ nanospheres/rGO	1 M KOH	128	[149]
	Conducting scaffold-supported 3D rGO-CNT/MoS_2 nanostructure	0.5 M H_2SO_4	123 @ 100 mA cm^{-2}	[150]
	Conducting scaffold-supported 3D rGO-CNT/MoS_2 nanostructure	1 M KOH	217 @ 50 mA cm^{-2}	[150]
	3D Pd nanosponge-shaped networks wrapped by graphene dots	0.5 M H_2SO_4	32	[151]
	3D graphene hollow nanospheres supported ruthenium phosphides	1 M KOH	25.5	[152]
	Ru Nanoclusters/N-graphene	1 M KOH	25.6	[153]
	FeCoNiB@Boron-doped vertically aligned graphene arrays	1 M KOH	31	[154]
	Plasma-etched, S-doped graphene	0.5 M H_2SO_4	178	[155]
	3D porous NG derivative integrated MoS_2 nanosheet	0.5 M H_2SO_4	157	[156]
	3D FeP NT/PG	0.5 M H_2SO_4	69	[157]
	A self-supporting P-Fe_3O_4@3DG bulk composite	1 M KOH	123	[158]
	Ni_2P nanoparticles/N,B-graphene	1 M KOH	92	[159]
	Dispersed tungsten (W)-optimized MoP nanoparticles on N,P-doped graphene oxide	1 M KOH	70	[160]
	Ni-Ni_3P@NPC/rGO	0.5 M H_2SO_4	113 @ 20 mA cm^{-2}	[161]
	Cobalt phosphide decorated/N,B-3D-graphene	0.5 M H_2SO_4	118	[162]
TMDs	V-SACs@ 1T-WS_2	0.5 M H_2SO_4	185	[163]
	NiS@ MoS_2-20	1 M KOH	146	[164]
	MoS_2/GO	0.5 M H_2SO_4	13.1	[165]
	VS_2@V_2C	1 M KOH	138	[166]
LDHs	Ni_2Cr_1-LDH	1 M KOH	67	[167]
	Co_2Mn_1-DH	1 M KOH	187	[168]
	V-Ce/CoFe LDH	1M KOH	73	[169]
g-C_3N_4	g-C_3N_4/FeS_2/MoS_2	0.5 M H_2SO_4	193	[170]

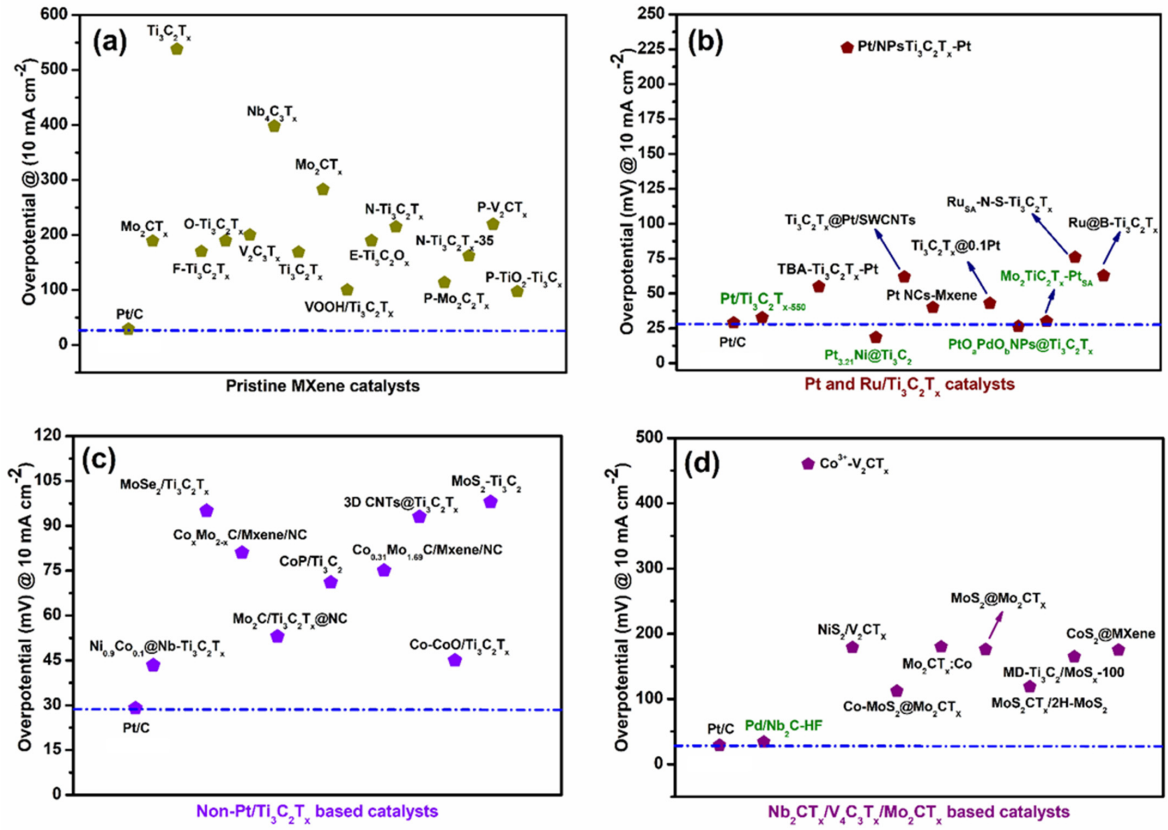

Figure 13. Benchmark figure (**a**) pristine MXene (**b**) Pt-supported $Ti_3C_2T_x$ (**c**) non-precious metal supported $Ti_3C_2T_x$ (**d**) Pt and non-precious metal supported on other types of MXenes, other than $Ti_3C_2T_x$ showing the overpotential status of various MXene-based catalysts with respect to standard Pt/C (for overpotential values of the catalysts, refer to Table 2. The Pt/C reference values were taken from Ref. [102]).

7. Conclusions and Future Perspectives

As a "rising star", MXene-based catalysts have been emerging as potential materials for electrocatalytic hydrogen evolution reaction. The unique 2D structure, chemical, surface and electronic properties provide tremendous opportunities to explore MXens for various electrochemical reactions, including HER. A number of families of MXenes are currently being explored for HER electrocatalysis, which include N-doped MXenes, surface-functionalized MXenes, Ti, V, Nb and Mo based MXenes. Among them, Mo and Ti based MXenes showed better HER activities, which can be further improved by developing effective synthesis strategies, by surface modification, lattice substitution, modulating the defects and controlling the morphology of the supported metal nanoparticles. Among the various surface functional groups (-OH, -O and -F), the -F terminations are found to be important and essential for HER kinetics. Therefore, adjusting the surface functional groups on MXenes might have a direct effect on the HER kinetics. Various Pt and non -Pt metal nanoparticles deposited MXenes were investigated. Among them, Pt-supported MXenes showed excellent HER activity, surpassing the commercial, benchmarking Pt/C catalyst in acidic electrolytes (in a few studies). However, non-Pt-supported MXenes, heteroatom-doped MXenes still showed lower HER kinetics, resulting in high overpotential.

In addition, a number of problems exist in the commercialization aspects of MXene-based electrocatalysts.

1. For example, the high surface energy of 2D MXene leads to re-stacking and agglomeration during catalyst synthesis. Re-stacking reduces the active surface area that needs to be exposed during electrochemical reactions. Therefore, avoiding re-stacking is one of the important factors for obtaining desirable HER activity. The use of intercalating

agents, such as large-sized organic molecules, use of ionic surfactants and conducting polymers are some of the strategies.

2. The productivity of the obtained MXenes is highly dependent on the type of synthesis process used, the composition and the number of layers. Further, MXene spontaneous oxidation or thermal-induced structural transformation to TiO_2 are some of the critical problems that need to be addressed.
3. Increasing MXenes' intrinsic activity is one of the important issues. Intrinsic activity depends on the type of metal atoms, density of C and N, and the type of surface functional groups and their interactions with the reaction intermediates is vital to obtain better catalysts. For example, -F and -OH functional groups are important for HER and other reactions, such as ORR and OER.
4. One of the major problems associated with MXenes lies in the synthesis process. For example, universally accepted fluoride etching is harmful to the environment and the structure of the MAX phases. The dissolved oxygen present in the aqueous HF can impart structural defects and promote their degradation into TiO_2.
5. Alternative synthesis strategies, such as electrochemical etching, produce a low yield, and molten salt requires high temperature, making it difficult to industrialize.
6. Careful tuning and reproducible density of surface functional groups are very difficult to achieve due to the fact that the type and density of surface functional groups highly depend on the type of the etchant and reaction conditions.

Despite the excellent progress, MXene-based electrocatalysts are in the nascent stage. The following strategies are recommended for improved HER kinetics of MXenes.

1. Strategies for controlling surface functional groups, creating porous structures, heteroatom doping, thereby optimizing the electronic and surface properties for selective HER kinetics, should be discovered.
2. Efforts are needed to increase the electronic conductivity of pristine MXenes by producing composite structures with carbon, graphene or by coating of the carbon on MXenes layers, by making 3D architectures that can act as ideal support for dispersing metal nanoparticles and creating interstitial pores for enhancing mass transport issues.
3. It is important to develop 3D porous network structures in MXene and MXenes-composite catalysts to enhance the mass transport properties of the catalysts.
4. While processing the MXenes is also one of the difficult tasks, as the MXenes are sensitive to oxidation, controlled etching, flake structure and heat treatment are required. Treating MXenes at higher temperatures leads to structural transformation of MXenes; for example, $Ti_3C_2T_x$ converts into TiO_2 upon heat treatment. Novel synthesis protocols are badly needed for processing MXenes at high temperatures.
5. Environmentally friendly etching processes need to be developed with a high yield and low structural defects. The currently used HF etching is found to be environmentally unfriendly, owing to the acute toxicity of HF.
6. Studies are required to find out if any pre-processing of the MAX phases has any effect on the subsequent etching step.
7. Efforts are needed to understand the effect of surface functionalities (other than -F, -OH and -O), such as -Cl, -Br, -I, -S, -B, -P, -Se, -Te, etc., on the HER activity of MXenes.
8. The durability of MXenes needs to be investigated in long-term operations. Most of the studies performed short-term stability tests, which cannot be guaranteed for long-term cycling operations. DFT calculations explored a number of possible MXenes catalysts as potential candidates for HER, especially the $M'_2M''CNO_2$ type of catalysts. Therefore, it is an interesting task for the experimental scientists to synthesize and study the $M'_2M''CNO_2$ type of MXenes experimentally in order to validate the DFT studies.
9. Advanced strategies, such as lattice substitution of M and X, metal-ion/non-metal ion substitution, defect engineering, morphology control, constructing stable heterojunctions of MXenes with other carbon and conductive 2D materials, are some of the approaches that can be explored.

With increased attention and continuous research evidenced by the rapidly increasing publications on MXenes, there is no doubt that MXene electrocatalysts will gather pace and will be explored for practical HER applications in the near future.

Author Contributions: Conceptualization, methodology, S.G.P. and R.K.; validation, formal analysis, G.R.; writing—original draft preparation, S.G.P. and R.K.; writing—review and editing, L.C., L.S. and G.M.; funding acquisition, S.G.P. and G.R. All authors have read and agreed to the published version of the manuscript.

Funding: This research is supported by the National Research Foundation of Korea (NRF) funded by the Korean government, Ministry of Science and ICT (MSIT) (Grant No. 2021R1F1A1046648), Republic of Korea. Dr. Gaddam Rajeshkhanna would like to acknowledge the Science and Engineering Research Board (SERB), Department of Science and Technology (DST), India (sanction order no: SRG/2021/001028) for providing the funding. Author, Liu Chao, acknowledge Natural Science Foundation of Jiangxi Province (Grant no. 20212BCJL23053 and 20212BAB203015), the Research Foundation of the Education, Department of Jiangxi Province (Grant no. GJJ200808) for funding this research.

Institutional Review Board Statement: Not applicable.

Informed Consent Statement: Not applicable.

Data Availability Statement: Not applicable.

Conflicts of Interest: The authors declare no conflict of interest.

References

1. Chu, S.; Majumdar, A. Opportunities and challenges for a sustainable energy future. *Nature* **2012**, *488*, 294–303. [CrossRef] [PubMed]
2. Zhang, Y.; Luo, M.; Yang, y.; Li, Y.; Guo, S. Advanced multifunctional electrocatalysts for energy conversion. *ACS Energy Lett.* **2019**, *4*, 1672–1680. [CrossRef]
3. York, R. Do alternative energy sources displace fossil fuels? *Nat. Clim. Change* **2012**, *2*, 441–443. [CrossRef]
4. Peera, S.G.; Liu, C. Unconventional and scalable synthesis of non-precious metal electrocatalysts for practical proton exchange membrane and alkaline fuel cells: A solid-state co-ordination synthesis approach. *Coord. Chem. Rev.* **2022**, *463*, 214554. [CrossRef]
5. Cai, Z.; Bu, X.; Wang, P.; Ho, J.C.; Yang, J.; Wang, X. Recent advances in layered double hydroxide electrocatalysts for the oxygen evolution reaction. *J. Mater. Chem. A* **2019**, *7*, 5069–5089. [CrossRef]
6. Holladay, J.D.; Hu, J.; King, D.L.; Wang, Y. An overview of hydrogen production technologies. *Catal. Today* **2019**, *139*, 244–260. [CrossRef]
7. Vazhayil, A.; Vazhayal, L.; Thomas, J.; Ashok, C.; Thomas, N. A comprehensive review on the recent developments in transitionmetal-based electrocatalysts for oxygen evolution reaction. *Appl. Surf. Sci. Adv.* **2021**, *6*, 100184. [CrossRef]
8. Li, X.; Zhao, L.; Yu, J.; Liu, X.; Zhang, X.; Liu, H.; Zhou, W. Water Splitting: From Electrode to Green Energy System. *Nanomicro. Lett.* **2020**, *12*, 131. [CrossRef]
9. Peera, S.G.; Koutavarapu, R.; Liu, C.; Rajeshkhanna, G.; Asokan, A.; Reddy, C.V. Cobalt Nanoparticle-Embedded Nitrogen-Doped Carbon Catalyst Derived from a Solid-State Metal-Organic Framework Complex for OER and HER Electrocatalysis. *Energies* **2021**, *14*, 1320. [CrossRef]
10. You, B.; Sun, Y. Innovative Strategies for Electrocatalytic Water Splitting. *Acc. Chem. Res.* **2018**, *51*, 1571–1580. [CrossRef]
11. Lee, J.E.; Jeon, K.J.; Show, P.L.; Leed, I.H.; Jung, S.C.; Choi, Y.J.; Rhee, G.H.; Lin, K.Y.A.; Park, Y.K. Mini review on H_2 production from electrochemical water splitting according to special nanostructured morphology of electrocatalysts. *Fuel* **2022**, *308*, 122048. [CrossRef]
12. Anantharaj, S.; Ede, S.R.; Sakthikumar, K.; Karthick, K.; Mishra, S.; Kundu, S. Recent Trends and Perspectives in Electrochemical Water Splitting with an Emphasis on Sulfide, Selenide, and Phosphide Catalysts of Fe, Co, and Ni: A Review. *ACS Catal.* **2016**, *6*, 8069–8097. [CrossRef]
13. Hwapyung, J.; Arun, K.; Arindam, A.; Rajkumar, P.; Subrata, K. Graphene-based materials as electrocatalysts for the oxygen evolution reaction: A review. *Sustain. Energy Fuels* **2022**, *6*, 640–663.
14. Qin, X.; Ola, O.; Zhao, J.; Yang, Z.; Tiwari, S.K.; Wang, N.; Zhu, Y. Recent Progress in Graphene-Based Electrocatalysts for Hydrogen Evolution Reaction. *Nanomaterials* **2022**, *12*, 1806. [CrossRef]
15. Zhou, D.; Li, P.; Lin, X.; McKinley, A.; Kuang, Y.; Liu, W.; Lin, W.-F.; Sun, X.; Duan, X. Layered double hydroxide-based electrocatalysts for the oxygen evolution reaction: Identification and tailoring of active sites, and superaerophobic nanoarray electrode assembly. *Chem. Soc. Rev.* **2021**, *50*, 8790–8817.
16. Xingshuai, L.; Wei, W.; Hao, W.; Baibiao, H.; Ying, D. Holey graphitic carbon nitride (g-CN) supported bifunctional single atom electrocatalysts for highly efficient overall water splitting. *Appl. Catal. B Environ.* **2020**, *264*, 118521.

17. Wang, F.; Shifa, T.A.; Zhan, X.; Huang, Y.; Liu, K.; Cheng, Z.; Jiang, C.; He, J. Recent advances in transition-metal dichalcogenide based nanomaterials for water splitting. *Nanoscale* **2015**, *7*, 19764–19788. [CrossRef]
18. Shinagawa, T.; Garcia-Esparza, A.T.; Takanabe, K. Insight on Tafel slopes from a microkinetic analysis of aqueous electrocatalysis for energy conversion. *Sci. Rep.* **2015**, *5*, 13801. [CrossRef]
19. Luo, Y.; Wang, S.; Ren, K.; Chou, J.P.; Yu, J.; Sun, Z.; Sun, M. Transition-metal dichalcogenides/$Mg(OH)_2$ van der waals heterostructures as promising water-splitting photocatalysts: A first-principles study. *Phys. Chem. Chem. Phys.* **2019**, *21*, 1791–1796. [CrossRef]
20. Seh, Z.W.; Kibsgaard, J.; Dickens, C.F.; Chorkendorff, I.; Nørskov, J.K.; Jaramillo, T.F. Combining theory and experiment in electrocatalysis: Insights into materials design. *Science* **2017**, *355*, 4998. [CrossRef] [PubMed]
21. Sui, X.; Zhang, L.; Li, J.; Davis, K.D.; Li, R.; Wang, Z.; Sun, X. Advanced Support Materials and Interactions for Atomically Dispersed Noble-Metal Catalysts: From Support Effects to Design Strategies. *Adv. Energy Mater.* **2022**, *12*, 2102556. [CrossRef]
22. Peera, S.G.; Kwon, H.J.; Lee, T.G.; Hussain, A.M. Heteroatom- and metalloid-doped carbon catalysts for oxygen reduction reaction: A mini-review. *Ionics* **2020**, *26*, 1563–1589. [CrossRef]
23. Peera, S.G.; Arunchander, A.; Sahu, A.K. Cumulative effect of transition metals on nitrogen and fluorine co-doped graphite nanofibers: An efficient and highly durable non-precious metal catalyst for the oxygen reduction reaction. *Nanoscale* **2016**, *8*, 14650–14664. [CrossRef] [PubMed]
24. Huanyu, J.; Xin, L.; Shuangming, C.; Anthony, V.; Laiquan, L.; Yan, J.; Li, S.; Yao, Z.; Shi-Zhang, Q. Heteroatom-Doped Transition Metal Electrocatalysts for Hydrogen Evolution Reaction. *ACS Energy Lett.* **2019**, *4*, 805–810.
25. Yan, J.; Yao, Z.; Kenneth, D.; Shi-Zhang, Q. Activity origin and catalyst design principles for electrocatalytic hydrogen evolution on heteroatom-doped graphene. *Nat. Energy* **2016**, *1*, 16130.
26. Srinu, A.; Parthiban, V.; Gouse Peera, S.; Singh, B.P.; Dhakate, S.R.; Sahu, A.K. Simultaneous Co-Doping of Nitrogen and Fluorine into MWCNTs: An In-Situ Conversion to Graphene Like Sheets and Its Electro-Catalytic Activity toward Oxygen Reduction Reaction. *J. Electrochem. Soc.* **2017**, *164*, F568.
27. Peera, S.G.; Koutavarapu, R.; Akula, S.; Asokan, A.; Moni, P.; Selvaraj, M.; Balamurugan, J.; Kim, S.O.; Liu, C.; Sahu, A.K. Carbon Nanofibers as Potential Catalyst Support for Fuel Cell Cathodes: A Review. *Energy Fuels* **2021**, *35*, 11761–11799. [CrossRef]
28. Shi, Y.; Ma, Z.R.; Xiao, Y.Y.; Yin, Y.C.; Huang, W.M.; Huang, Z.C.; Zheng, Y.Z.; Mu, F.Y.; Huang, R.; Shi, G.Y.; et al. Electronic metal–support interaction modulates single-atom platinum catalysis for hydrogen evolution reaction. *Nat. Commun.* **2021**, *12*, 3021. [CrossRef]
29. Oh, H.S.; Nong, H.N.; Reier, T.; Bergmann, A.; Gliech, M.; de Araújo, J.F.; Willinger, E.; Schlögl, R.; Teschner, D.; Strasser, P. Electrochemical Catalyst—Support Effects and Their Stabilizing Role for IrOx Nanoparticle Catalysts during the Oxygen Evolution Reaction. *J. Am. Chem. Soc.* **2016**, *138*, 12552–12563. [CrossRef]
30. Peera, S.G.; Liu, C.; Sahu, A.K.; Selvaraj, M.; Rao, M.C.; Lee, T.G.; Koutavarapu, R.; Shim, J.; Singh, L. Recent Advances on MXene-Based Electrocatalysts toward Oxygen Reduction Reaction: A Focused Review. *Adv. Mater. Interfaces* **2021**, *8*, 2100975. [CrossRef]
31. Peera, S.G.; Liu, C.; Shim, J.; Sahu, A.K.; Lee, T.G.; Selvaraj, M.; Koutavarapu, M. MXene (Ti_3C_2Tx) supported electrocatalysts for methanol and ethanol electrooxidation: A review. *Ceram. Int.* **2021**, *47*, 28106–28121. [CrossRef]
32. Zhu, H.; Xue, S.; Liang, Z.; Liang, X.; Li, G.; Ren, X.; Gao, L.; Li, Q.; Ma, T.; Liu, A. Self-assembly synthesis of Ni-decorated Nb_2C MXene as an efficient and stable catalyst towards electrochemical nitrogen reduction. *Ceram. Int.* **2022**, *48*, 20599–20604.
33. Soomro, R.A.; Jawaid, S.; Zhu, Q.; Abbas, Z.; Xu, B. A mini review on MXenes as versatile substrate for advanced sensors, Chin. *Chem. Lett.* **2020**, *31*, 922–930.
34. Xu, B.; Ye, F.; Chen, R.; Luo, X.; Chang, G.; Li, R. A wide sensing range and high sensitivity flexible strain sensor based on carbon nanotubes and MXene. *Ceram. Int.* **2022**, *48*, 10220–10226. [CrossRef]
35. Bai, S.; Yang, M.; Jiang, J.; He, X.; Zou, J.; Xiong, Z.; Liao, G.; Liu, S. Recent advances of MXenes as electrocatalysts for hydrogen evolution reaction. *NPJ 2D Mater. Appl.* **2021**, *5*, 78. [CrossRef]
36. Liu, J.; Peng, W.; Li, Y.; Zhang, F.; Fan, X. 2D MXene-Based Materials for Electrocatalysis. *Trans. Tianjin Univ.* **2020**, *26*, 149–171. [CrossRef]
37. González-Poggini, S.; Rosenkranz, A.; Colet-Lagrille, M. Two-Dimensional Nanomaterials for the Removal of Pharmaceuticals from Wastewater: A Critical Review. *Processes* **2021**, *9*, 2160. [CrossRef]
38. Brian, C. Wyatt, Andreas Rosenkranz, Babak Anasori, 2D MXenes: Tunable Mechanical and Tribological Properties. *Adv. Mater.* **2021**, *33*, 2007973.
39. Maibelin, R.; Andreina, G.; Victor, M.F.; Rodrigo, E.-G.; Guichen, S.; Bo, W.; Jinhong, Y.; Francisco, G.; Andreas, R. Unprecedented arsenic photo-oxidation behavior of few- and multi-layer $Ti_3C_2T_x$ nano-sheets. *Appl. Mater. Today* **2020**, *20*, 100769.
40. Elodie, B.; Andreas, R.; Rodrigo, E.-G.; Victor, M.F.; Zhenyu, Z.; Sebastián, S.; Néstor, E. Catalytic performance of 2D-Mxene nano-sheets for the hydrodeoxygenation (HDO) of lignin-derived model compounds. *Catal. Commun.* **2020**, *133*, 105833.
41. Gogotsi, Y.; Anasori, B. The Rise of MXenes. *ACS Nano.* **2019**, *13*, 8491–8494. [CrossRef] [PubMed]
42. Kim, Y.J.; Kim, S.J.; Seo, D.; Chae, Y.; Anayee, M.; Lee, Y.; Gogotsi, Y.; Ahn, C.W.; Jung, H.T. Etching Mechanism of Monoatomic Aluminum Layers during MXene Synthesis. *Chem. Mater.* **2021**, *33*, 6346–6355. [CrossRef]
43. Sang, X.; Xie, Y.; Lin, M.W.; Alhabeb, M.; Aken, K.L.V.; Gogotsi, Y.; Kent, P.R.C.; Xiao, K.; Unocic, R.R. Atomic Defects in Monolayer Titanium Carbide (Ti3C2Tx) MXene. *ACS Nano.* **2016**, *10*, 9193–9200. [CrossRef]

44. Ashton, M.; Mathew, K.; Hennig, R.G.; Sinnott, S.B. Predicted Surface Composition and Thermodynamic Stability of MXenes in Solution. *J. Phys. Chem. C* **2016**, *120*, 3550–3556. [CrossRef]
45. Jesus, G.-J. Processing of MAX phases: From synthesis to applications. *J. Am. Ceram. Soc.* **2021**, *104*, 659–690.
46. Rodrigo, M.R.; Jeverson, T.A.; Sydney, F.S. Synthesis, structure, properties and applications of MXenes: Current status and perspectives. *Ceram. Int.* **2019**, *45*, 18167–18188.
47. Pogorielov, M.; Smyrnova, K.; Kyrylenko, S.; Gogotsi, O.; Zahorodna, V.; Pogrebnjak, A. MXenes—A New Class of Two-Dimensional Materials: Structure, Properties and Potential Applications. *Nanomaterials* **2021**, *11*, 3412. [CrossRef]
48. Hu, T.; Hu, M.; Gao, B.; Li, W.; Wang, X. Screening Surface Structure of MXenes by High-Throughput Computation and Vibrational Spectroscopic Confirmation. *J. Phys. Chem. C* **2018**, *122*, 18501–18509. [CrossRef]
49. Persson, P.O.A.; Rosen, J. Current state of the art on tailoring the MXene composition, structure, and surface chemistry. *Curr Opin. Solid State Mater Sci.* **2019**, *23*, 100774. [CrossRef]
50. Mohammad, M.; Masoud, S. Surface functionalization of MXenes. *Mater. Adv.* **2021**, *2*, 7277–7307.
51. Rina, I.; Paul, E.; Patrick, R.; Hannu-Pekka, K. Surface Functionalization of 2D MXenes: Trends in Distribution, Composition, and Electronic Properties. *J. Phys. Chem. Lett.* **2021**, *12*, 2377–2384.
52. Aamir, I.; Junpyo, H.; Tae, Y.K.; Chong, M.K. Improving oxidation stability of 2D MXenes: Synthesis, storage media, and conditions. *Nano. Converg.* **2021**, *8*, 9.
53. Halim, J.; Cook, K.M.; Naguib, M.; Eklund, P.; Gogotsi, Y.; Rosen, J.; Barsoum, M.W. X-ray photoelectron spectroscopy metal of select multi-layered transition carbides (MXenes). *Appl. Surf. Sci.* **2016**, *362*, 406–417. [CrossRef]
54. Li, X.; Huang, Z.; Zhi, C. Environmental Stability of MXenes as Energy Storage Materials. *Front. Mater.* **2019**, *6*, 312–321. [CrossRef]
55. Zhang, C.J.; Pinilla, S.; McEvoy, N.; Cullen, C.P.; Anasori, B.; Long, E.; Park, S.H.; Ascaso, A.S.; Shmeliov, A.; Krishnan, D.; et al. Oxidation Stability of Colloidal Two-Dimensional Titanium Carbides (MXenes). *Chem. Mater.* **2017**, *29*, 4848–4856. [CrossRef]
56. Halim, J.; Persson, I.; Eklund, P.; Persson, P.O.A.; Rosen, J. Sodium hydroxide and vacuum annealing modifications of the surface terminations of a Ti_3C_2 (MXene) epitaxial thin film. *RSC Adv.* **2018**, *8*, 36785–36790. [CrossRef]
57. Dall'Agnese, Y.; Lukatskaya, M.R.; Cook, K.M.; Taberna, P.L.; Gogotsi, Y.; Simon, P. High capacitance of surface-modified 2D titanium carbide in acidic electrolyte. *Electrochem. Comm.* **2014**, *48*, 118–122. [CrossRef]
58. Persson, I.; Näslund, L.A.; Halim, J.; Barsoum, M.W.; Darakchieva, V.; Palisaitis, J.; Rosen, J.; Persson, P.O.A. On the organization and thermal behavior of functional groups on Ti_3C_2 MXene surfaces in vacuum. *2D Mater.* **2017**, *5*, 015002. [CrossRef]
59. Hart, J.L.; Hantanasirisakul, K.; Lang, A.C.; Anasori, B.; Pinto, D.; Pivak, Y.; van Omme, J.T.; May, S.Y.; Gogotsi, Y.; Taheri, M.L. Control of MXenes' electronic properties through termination and intercalation. *Nat. Commun.* **2019**, *10*, 522. [CrossRef]
60. Parra-Puerto, A.; Ng, K.L.; Fahy, K.; Goode, A.E.; Ryan, M.P.; Kucernak, A. Supported transition metal phosphides: Activity survey for HER, ORR, OER and corrosion resistance in acid and alkaline electrolytes. *ACS Catal.* **2019**, *9*, 11515–11529. [CrossRef]
61. Hao, C.; Wu, Y.; An, Y.; Cui, B.; Lin, J.; Li, X.; Wang, D.; Jiang, M.; Cheng, Z.; Hu, S. Interface-coupling of CoFe-LDH on MXene as high-performance oxygen evolution catalyst. *Mater. Today Energy* **2019**, *12*, 453–462. [CrossRef]
62. Fu, G.; Lee, J.-M. Ternary metal sulfides for electrocatalytic energy conversion. *J. Mater. Chem. A* **2019**, *7*, 9386–9405. [CrossRef]
63. Peng, X.; Pi, C.; Zhang, X.; Li, S.; Huo, K.; Chu, P.K. Recent progress of transition metal nitrides for efficient electrocatalytic water splitting. *Sustain. Energ. Fuels* **2019**, *3*, 366–381. [CrossRef]
64. Zhu, Y.; Liu, X.; Jin, S.; Chen, H.; Lee, W.; Liu, M.; Chen, Y. Anionic defect engineering of transition metal oxides for oxygen reduction and evolution reactions. *J. Mater. Chem. A* **2019**, *7*, 5875–5897. [CrossRef]
65. Peera, S.G.; Arunchander, A.; Sahu, A.K. Platinum nanoparticles supported on nitrogen and fluorine co-doped graphite nanofibers as an excellent and durable oxygen reduction catalyst for polymer electrolyte fuel cells. *Carbon* **2016**, *107*, 667–679. [CrossRef]
66. Peera, S.G.; Sahu, A.K.; Arunchander, A.; Nath, K.; Bhat, S.D. Deoxyribonucleic acid directed metallization of platinum nanoparticles on graphite nanofibers as a durable oxygen reduction catalyst for polymer electrolyte fuel cells. *J. Power Sources* **2015**, *297*, 379–387. [CrossRef]
67. Wu, X.; Kang, F.; Duan, W.; Li, J. Density functional theory calculations: A powerful tool to simulate and design high-performance energy storage and conversion materials. *Prog. Nat. Sci. Mater. Int.* **2019**, *29*, 247–255. [CrossRef]
68. Bai, X.; Ling, C.; Shi, L.; Ouyang, Y.; Li, Q.; Wang, J. Insight into the catalytic activity of MXenes for hydrogen evolution reaction. *Sci. Bull.* **2018**, *63*, 1397–1403. [CrossRef]
69. Huang, B.; Zhou, N.; Chen, X.; Ong, W.; Li, N. Insights into the Electrocatalytic Hydrogen Evolution Reaction Mechanism on Two-Dimensional Transition-Metal Carbonitrides (MXene). *Chem. A Eur. J.* **2018**, *24*, 18479–18486. [CrossRef]
70. Jin, D.; Johnson, L.R.; Raman, A.S.; Ming, X.; Gao, Y.; Du, F.; Wei, Y.; Chen, G.; Vojvodic, A.; Gogotsi, Y.; et al. Computational Screening of 2D Ordered Double Transition-Metal Carbides (MXenes) as Electrocatalysts for Hydrogen Evolution Reaction. *J. Phys. Chem. C* **2020**, *124*, 10584–10592. [CrossRef]
71. Zeng, Z.; Chen, X.; Weng, K.; Wu, Y.; Zhang, P.; Jiang, J.; Li, N. Computational screening study of double transition metal carbonitrides $M'_2M''CNO_2$-MXene as catalysts for hydrogen evolution reaction. *NPJ Comput. Mater.* **2021**, *7*, 80. [CrossRef]
72. Wang, X.; Wang, C.; Ci, S.; Ma, Y.; Liu, T.; Gao, L.; Qian, P.; Ji, C.; Su, Y. Accelerating 2D MXene catalyst discovery for the hydrogen evolution reaction by computer-driven workflow and an ensemble learning strategy. *J. Mater. Chem. A* **2020**, *8*, 23488–23497. [CrossRef]

73. Zheng, J.; Sun, X.; Qiu, C.; Yan, Y.; Yao, Z.; Deng, S.; Zhong, X.; Zhuang, G.; Wei, Z.; Wang, J. High-Throughput Screening of Hydrogen Evolution Reaction Catalysts in MXene Materials. *J. Phys. Chem. C* **2020**, *124*, 13695–13705. [CrossRef]
74. Akshay Kumar, K.P.; Alduhaish, O.; Pumera, M. Electrocatalytic activity of layered MAX phases for the hydrogen evolution reaction. *Electrochem. Commun.* **2021**, *125*, 106977. [CrossRef]
75. Li, S.; Tuo, P.; Xie, J.; Zhang, X.; Xu, J.; Bao, J.; Pan, B.; Xie, Y. Ultrathin MXene nanosheets with rich fluorine termination groups realizing efficient electrocatalytic hydrogen evolution. *Nano Energy* **2018**, *47*, 512–518. [CrossRef]
76. Zhang, S.; Zhuo, H.; Li, S.; Bao, Z.; Deng, S.; Zhuang, G.; Zhong, X.; Wei, Z.; Yao, Z.; Wang, J. Effects of surface functionalization of mxene-based nanocatalysts on hydrogen evolution reaction performance. *Catal. Today* **2021**, *368*, 187–195. [CrossRef]
77. Yoon, Y.; Tiwari, A.P.; Lee, M.; Choi, M.; Song, W.; Im, J.; Zyung, T.; Jung, H.-K.; Lee, S.S.; Jeon, S.; et al. Enhanced electrocatalytic activity by chemical nitridation of two-dimensional titanium carbide MXene for hydrogen evolution. *J. Mater. Chem. A* **2018**, *6*, 20869–20877. [CrossRef]
78. Le, T.A.; Bui, Q.V.; Tran, N.Q.; Cho, Y.; Hong, Y.; Kawazoe, Y.; Lee, H. Synergistic Effects of Nitrogen Doping on MXene for Enhancement of Hydrogen Evolution Reaction. *ACS Sustain. Chem. Eng.* **2019**, *7*, 16879–16888. [CrossRef]
79. Han, M.; Yang, J.; Jiang, J.; Jing, R.; Ren, S.; Yan, C. Efficient tuning the electronic structure of N-doped Ti-based MXene to enhance hydrogen evolution reaction. *J. Colloid Interface Sci.* **2021**, *582*, 1099–1106. [CrossRef]
80. Zhang, X.; Shao, B.; Sun, Z.; Gao, Z.; Qin, Y.; Zhang, C.; Cui, F.; Yang, X. Platinum Nanoparticle-Deposited Ti_3C_2Tx MXene for Hydrogen Evolution Reaction. *Ind. Eng. Chem. Res.* **2020**, *59*, 1822–1828. [CrossRef]
81. Yuan, Y.; Li, H.; Wang, L.; Zhang, L.; Shi, D.; Hong, Y.; Sun, J. Achieving Highly Efficient Catalysts for Hydrogen Evolution Reaction by Electronic State Modification of Platinum on Versatile $Ti_3C_2T_x$ (MXene). *ACS Sustain. Chem. Eng.* **2019**, *7*, 4266–4273. [CrossRef]
82. Wu, Y.; Wei, W.; Yu, R.; Xia, L.; Hong, X.; Zhu, J.; Li, J.; Lv, L.; Chen, W.Y.; Zhao, W.; et al. Anchoring Sub-Nanometer Pt Clusters on Crumpled Paper-Like MXene Enables High Hydrogen Evolution Mass Activity. *Adv. Funct. Mater.* **2022**, *32*, 2110910. [CrossRef]
83. Lu, S.; Lou, F.; Yu, Z. Recent Progress in Two-Dimensional Materials for Electrocatalytic CO_2 Reduction. *Catalysts* **2022**, *12*, 228. [CrossRef]
84. Lv, Z.; Ma, W.; Wang, M.; Dang, J.; Jian, K.; Liu, D.; Huang, D. Co-Constructing Interfaces of Multiheterostructure on MXene (Ti_3C_2Tx)-Modified 3D Self-Supporting Electrode for Ultraefficient Electrocatalytic HER in Alkaline Media. *Adv. Funct. Mater.* **2021**, *31*, 2102576. [CrossRef]
85. Han, S.; Chen, Y.; Hao, Y.; Xie, Y.; Xie, D.; Chen, Y.; Xiong, Y.; He, Z.; Hu, F.; Li, L.; et al. Multi-dimensional hierarchical CoS_2@MXene as trifunctional electrocatalysts for zinc-air batteries and overall water splitting. *Sci. China Mater.* **2020**, *64*, 1127–1138. [CrossRef]
86. Jiang, J.; Bai, S.; Yang, M.; Zou, J.; Li, N.; Peng, J.; Wang, H.; Xiang, K.; Liu, S.; Zhai, T. Strategic design and fabrication of MXenes-Ti_3CNCl_2@CoS_2 core–shell nanostructure for high-efficiency hydrogen evolution. *Nano Res.* **2022**, *15*, 5977–5986. [CrossRef]
87. Wang, P.; Pu, Z.; Li, W.; Zhu, J.; Zhang, C.; Zhao, Y.; Mu, S. Coupling $NiSe_2$-Ni_2P heterostructure nanowrinkles for highly efficient overall water splitting. *J. Catal.* **2019**, *377*, 600–608. [CrossRef]
88. Lv, Z.; Wang, M.; Liu, D.; Jian, K.; Zhang, R.; Dang, J. Synergetic Effect of Ni_2P and MXene Enhances Catalytic Activity in the Hydrogen Evolution Reaction. *Inorg. Chem.* **2021**, *60*, 1604–1611. [CrossRef]
89. Jiang, H.; Wang, Z.; Yang, Q.; Tan, L.; Dong, L.; Dong, M. Ultrathin $Ti_3C_2T_x$ (MXene) Nanosheet-Wrapped $NiSe_2$ Octahedral Crystal for Enhanced Supercapacitor Performance and Synergetic Electrocatalytic Water Splitting. *Nano-Micro Lett.* **2019**, *11*, 31. [CrossRef]
90. Du, C.F.; Sun, X.; Yu, H.; Liang, Q.; Dinh, K.N.; Zheng, Y.; Luo, Y.; Wang, Z.; Yan, Q. Synergy of Nb Doping and Surface Alloy Enhanced on Water–Alkali Electrocatalytic Hydrogen Generation Performance in Ti-Based MXene. *Adv. Sci.* **2019**, *6*, 1900116. [CrossRef]
91. Tan, Y.; Zhu, Z.; Zhang, X.; Zhang, J.; Zhou, Y.; Li, H.; Qin, H.; Bo, Y.; Pan, Z. $Nb_4C_3T_x$ (MXene) as a new stable catalyst for the hydrogen evolution reaction. *Int. J. Hydrogen Energy* **2021**, *46*, 1955–1966. [CrossRef]
92. Pang, S.Y.; Io, W.F.; Hao, J. Facile Atomic-Level Tuning of Reactive Metal–Support Interactions in the Pt QDs@HF-Free MXene Heterostructure for Accelerating pH-Universal Hydrogen Evolution Reaction. *Adv. Sci.* **2021**, *8*, 2102207. [CrossRef] [PubMed]
93. Fan, X.; Du, P.; Ma, X.; Wang, R.; Ma, J.; Wang, Y.; Fan, D.; Long, Y.; Deng, B.; Huang, K.; et al. Mechanochemical Synthesis of Pt/Nb_2CTx MXene Composites for Enhanced Electrocatalytic Hydrogen Evolution. *Materials* **2021**, *14*, 2426. [CrossRef] [PubMed]
94. Wu, M.; Wang, B.; Hu, Q.; Wang, L.; Zhou, A. The Synthesis Process and Thermal Stability of V_2C MXene. *Materials* **2018**, *11*, 2112. [CrossRef] [PubMed]
95. Ling, C.; Shi, L.; Ouyang, Y.; Chen, Q.; Wang, J. Transition Metal-Promoted V_2CO_2 (MXenes): A New and Highly Active Catalyst for Hydrogen Evolution Reaction. *Adv. Sci.* **2016**, *3*, 1600180. [CrossRef] [PubMed]
96. Tran, M.H.; Schäfer, T.; Shahraei, A.; Dürrschnabel, M.; Molina-Luna, L.; Kramm, U.I.; Birkel, C.S. Adding a New Member to the MXene Family: Synthesis, Structure, and Electrocatalytic Activity for the Hydrogen Evolution Reaction of V_4C_3Tx. *ACS Appl. Energy Mater.* **2018**, *1*, 3908–3914. [CrossRef]
97. Park, S.; Lee, Y.L.; Yoon, Y.; Park, S.Y.; Yim, S.; Song, W.; Myung, S.; Lee, K.S.; Chang, H.; Lee, S.S.; et al. Reducing the high hydrogen binding strength of vanadium carbide MXene with atomic Pt confinement for high activity toward HER. *Appl. Catal. B Environ.* **2022**, *304*, 120989. [CrossRef]

98. Yoon, Y.; Tiwari, A.P.; Choi, M.; Novak, T.G.; Song, W.; Chang, H.; Zyung, T.; Lee, S.S.; Jeon, S.; An, K.S. Precious-Metal-Free Electrocatalysts for Activation of Hydrogen Evolution with Nonmetallic Electron Donor: Chemical Composition Controllable Phosphorous Doped Vanadium Carbide MXene. *Adv. Funct. Mater.* **2019**, *29*, 1903443. [CrossRef]
99. Kuznetsov, D.A.; Chen, Z.; Kumar, P.V.; Tsoukalou, A.; Kierzkowska, A.; Abdala, P.M.; Safonova, O.V.; Fedorov, A.; Müller, C.R. Single Site Cobalt Substitution in 2D Molybdenum Carbide (MXene) Enhances Catalytic Activity in the Hydrogen Evolution Reaction. *J. Am. Chem. Soc.* **2019**, *141*, 17809–17816. [CrossRef]
100. Liu, S.; Lin, Z.; Wan, R.; Liu, Y.; Liu, Z.; Zhang, S.; Zhang, X.; Tang, Z.; Lu, X.; Tian, Y. Cobalt phosphide supported by two-dimensional molybdenum carbide (MXene) for the hydrogen evolution reaction, oxygen evolution reaction, and overall water splitting. *J. Mater. Chem. A* **2021**, *9*, 21259–21269. [CrossRef]
101. Tan, Y.; Yi, M.; Zhu, Z.; Zhang, X.; Qin, K.; Zhang, J.; Zhu, R. Carbon-coated $MoSe_2/Mo_2CT_x$ (MXene) heterostructure for efficient hydrogen evolution. *Mater. Sci. Eng. B* **2021**, *271*, 115239. [CrossRef]
102. Lim, K.R.G.; Handoko, A.D.; Johnson, L.R.; Meng, X.; Lin, M.; Subramanian, G.S.; Anasori, B.; Gogotsi, Y.; Vojvodic, A.; She, Z.W. 2H-MoS_2 on Mo_2CT_x MXene Nanohybrid for Efficient and Durable Electrocatalytic Hydrogen Evolution. *ACS Nano* **2020**, *14*, 16140–16155. [CrossRef] [PubMed]
103. Ren, J.; Zong, H.; Sun, Y.; Gong, S.; Feng, Y.; Wang, Z.; Hu, L.; Yu, K.; Zhu, Z. 2D organ-like molybdenum carbide (MXene) coupled with MoS_2 nanoflowers enhances the catalytic activity in the hydrogen evolution reaction. *Cryst. Eng. Comm.* **2020**, *22*, 1395. [CrossRef]
104. Seh, Z.W.; Fredrickson, K.D.; Anasori, D.; Kibsgaard, J.; Strickler, A.L.; Lukatskaya, M.R.; Gogotsi, Y.; Jaramillo, T.F.; Vojvodic, A. Two-Dimensional Molybdenum Carbide (MXene) as an Efficient Electrocatalyst for Hydrogen Evolution. *ACS Energy Lett.* **2016**, *1*, 589–594. [CrossRef]
105. Handoko, A.D.; Fredrickson, K.D.; Anasori, B.; Convey, K.W.; Johnson, L.R.; Gogotsi, Y.; Vojvodic, A.; Seh, Z.W. Tuning the Basal Plane Functionalization of Two-Dimensional Metal Carbides (MXenes) To Control Hydrogen Evolution Activity. *ACS Appl. Energy Mater.* **2018**, *1*, 173–180. [CrossRef]
106. Jiang, Y.; Sun, T.; Xie, X.; Jiang, W.; Li, J.; Tian, B.; Su, C. Oxygen-Functionalized Ultrathin $Ti_3C_2T_x$ MXene for Enhanced Electrocatalytic Hydrogen Evolution. *ChemSusChem* **2019**, *12*, 1368. [CrossRef]
107. Yuan, W.; Cheng, L.; An, Y.; Wu, H.; Yao, N.; Fan, X.; Guo, X. MXene Nanofibers as Highly Active Catalysts for Hydrogen Evolution Reaction. *ACS Sustain. Chem. Eng.* **2018**, *6*, 8976–8982. [CrossRef]
108. Yan, L.; Chen, X.; Liu, X.; Chen, L.; Zhang, B. In situ VOOH nanosheet arrays formed anchored on a $Ti_3C_2T_x$ MXene as a highly efficient and robust synergistic electrocatalyst for boosting water oxidation and reduction. *J. Mater. Chem. A* **2020**, *8*, 23637–23644. [CrossRef]
109. Qu, G.; Zhou, Y.; Wu, T.; Zhao, G.; Li, F.; Kang, Y.; Xu, C. Phosphorized MXene-Phase Molybdenum Carbide as an Earth-Abundant Hydrogen Evolution Electrocatalyst. *ACS Appl. Energy Mater.* **2018**, *1*, 7206–7212. [CrossRef]
110. Deng, L.; Chang, B.; Shi, D.; Yao, X.; Shao, Y.; Shen, J.; Zhang, B.; Wu, Y.; Hao, X. MXene decorated by phosphorus-doped TiO2 for photo-enhanced electrocatalytic hydrogen evolution reaction. *Renew. Energy* **2021**, *170*, 858–865. [CrossRef]
111. Li, Z.; Qi, Z.; Wang, S.; Ma, T.; Zhou, L.; Wu, Z.; Luan, X.; Lin, F.; Chen, M.; Miller, J.T.; et al. In Situ Formed Pt3Ti Nanoparticles on a Two-Dimensional Transition Metal Carbide (MXene) Used as Efficient Catalysts for Hydrogen Evolution Reactions. *Nano Lett.* **2019**, *19*, 5102–5108. [CrossRef]
112. Filip, J.; Zavahir, S.; Lorencova, L.; Bertok, T.; Yousaf, A.B.; Mahmoud, K.A.; Tkac, J.; Kasak, P. Tailoring Electrocatalytic Properties of Pt Nanoparticles Grown on $Ti_3C_2T_x$ MXene Surface. *J. Electrochem. Soc.* **2019**, *166*, H54–H62. [CrossRef]
113. Jiang, Y.; Wu, X.; Yan, Y.; Luo, S.; Li, X.; Huang, J.; Zhang, H.; Yang, D. Coupling PtNi Ultrathin Nanowires with MXenes for Boosting Electrocatalytic Hydrogen Evolution in Both Acidic and Alkaline Solutions. *Small* **2019**, *15*, 1805474. [CrossRef]
114. Cui, C.; Cheng, R.; Zhang, H.; Zhang, C.; Ma, Y.; Shi, C.; Fan, B.; Wang, H.; Wang, X. Ultrastable MXene@Pt/SWCNTs' Nanocatalysts for Hydrogen Evolution Reaction. *Adv. Funct. Mater.* **2020**, *30*, 200693. [CrossRef]
115. Jian, X.; Wei, T.T.; Zhang, M.M.; Li, R.; Liu, J.X.; Liang, Z.H. Construction of $Ti_3C_2T_x$ MXene Supported Low-Platinum Electrocatalyst for Hydrogen Evolution Reaction by Direct Electrochemical Strategy. *J. Electrochem. Soc.* **2021**, *168*, 096504. [CrossRef]
116. Cui, C.; Cheng, R.; Zhang, C.; Wang, X. Pt immobilized spontaneously on porous MXene/MAX hybrid monolith for hydrogen evolution reaction. *Chin. Chem. Lett.* **2020**, *31*, 988–991. [CrossRef]
117. Cui, B.; Hu, B.; Liu, J.; Wang, M.; Song, Y.; Tian, K.; Zhang, Z.; He, L. Solution-Plasma-Assisted Bimetallic Oxide Alloy Nanoparticles of Pt and Pd Embedded within Two-Dimensional Ti3C2Tx Nanosheets as Highly Active Electrocatalysts for Overall Water Splitting. *ACS Appl. Mater. Interfaces* **2018**, *10*, 23858–23873. [CrossRef]
118. Zhang, J.; Zhao, Y.; Guo, X.; Chen, C.; Dong, C.L.; Liu, R.S.; Han, C.P.; Li, Y.; Gogotsi, Y.; Wang, G. Single platinum atoms immobilized on an MXene as an efficient catalyst for the hydrogen evolution reaction. *Nat. Catal.* **2018**, *1*, 985–992. [CrossRef]
119. Ramalingam, V.; Varadhan, P.; Fu, H.C.; Kim, H.; Zhang, D.; Chen, S.; Song, L.; Ma, D.; Wang, Y.; Alshareef, H.N.; et al. Hau. Heteroatom-Mediated Interactions between Ruthenium Single Atoms and an MXene Support for Efficient Hydrogen Evolution. *Adv. Mater.* **2019**, *31*, 1903841. [CrossRef] [PubMed]
120. Bat-Erdene, M.; Batmunkh, M.; Sainbileg, B.; Hayashi, M.; Bati, A.S.R.; Qin, J.; Zhao, H.; Zhong, Y.L.; Shapter, J.G. Highly Dispersed Ru Nanoparticles on Boron-Doped $Ti_3C_2T_x$ (MXene) Nanosheets for Synergistic Enhancement of Electrocatalytic Hydrogen Evolution. *Small* **2021**, *17*, 2102218. [CrossRef]

121. Pang, S.Y.; Wong, Y.T.; Yuan, S.; Liu, Y.; Tsang, M.K.; Yang, Z.; Huang, H.; Wong, W.T.; Hao, J. Universal Strategy for HF-Free Facile and Rapid Synthesis of Two-dimensional MXenes as Multifunctional Energy Materials. *J. Am. Chem. Soc.* **2019**, *141*, 9610–9616. [CrossRef] [PubMed]
122. Du, C.F.; Dinh, K.N.; Liang, Q.; Zheng, Y.; Luo, Y.; Zhang, J.; Yan, Q. Self-Assemble and In Situ Formation of $Ni_{1-x}Fe_xPS_3$ Nanomosaic-Decorated MXene Hybrids for Overall Water Splitting. *Adv. Energy Mater.* **2018**, *8*, 1801127. [CrossRef]
123. Wu, X.; Wang, Z.; Yu, M.; Xiu, L.; Qiu, J. Stabilizing the MXenes by Carbon Nanoplating for Developing Hierarchical Nanohybrids with Efficient Lithium Storage and Hydrogen Evolution Capability. *Adv. Mater.* **2017**, *29*, 1607017. [CrossRef] [PubMed]
124. Liu, J.; Liu, Y.; Xu, D.; Zhu, Y.; Peng, W.; Li, Y.; Zhang, F.; Fan, X. Hierarchical "nanoroll" like MoS_2/ $Ti_3C_2T_x$ hybrid with high electrocatalytic hydrogen evolution activity. *Appl. Catal. B Environ.* **2019**, *241*, 89–94. [CrossRef]
125. Xiu, L.; Wang, Z.; Yu, M.; Wu, X.; Qiu, J. Aggregation-Resistant 3D MXene-Based Architecture as Efficient Bifunctional Electrocatalyst for Overall Water Splitting. *ACS Nano.* **2018**, *12*, 8017–8028. [CrossRef]
126. Li, N.; Zhang, Y.; Jia, M.; Lv, X.; Li, X.; Li, R.; Ding, X.; Zheng, Y.Z.; Tao, X. 1T/2H $MoSe_2$-on-MXene heterostructure as bifunctional electrocatalyst for efficient overall water splitting. *Electrochim. Acta* **2019**, *326*, 134976. [CrossRef]
127. Wu, X.; Zhou, S.; Wang, Z.; Liu, J.; Pei, W.; Yang, P.; Zhao, J.; Qiu, J. Engineering Multifunctional Collaborative Catalytic Interface Enabling Efficient Hydrogen Evolution in All pH Range and Seawater. *Adv. Energy Mater.* **2019**, *9*, 1901333. [CrossRef]
128. Wang, H.; Lin, Y.; Liu, S.; Li, J.; Bu, L.; Chen, J.; Xiao, X.; Choi, J.H.; Gao, L.; Lee, J.M. Confined growth of pyridinic N-Mo_2C sites on MXenes for hydrogen evolution. *J. Mater. Chem. A* **2020**, *8*, 7109–7116. [CrossRef]
129. Yu, M.; Wang, Z.; Liu, J.; Sun, F.; Yang, P.; Qiu, J. A hierarchically porous and hydrophilic 3D nickel–iron/MXene electrode for accelerating oxygen and hydrogen evolution at high current densities. *Nano Energy* **2019**, *63*, 103880. [CrossRef]
130. Tang, Y.; Yang, C.; Sheng, M.; Yin, X.; Que, W. Synergistically Coupling Phosphorus-Doped Molybdenum Carbide with MXene as a Highly Efficient and Stable Electrocatalyst for Hydrogen Evolution Reaction. *ACS Sustain. Chem. Eng.* **2020**, *8*, 12990–12998. [CrossRef]
131. Yan, L.; Zhang, B.; Wu, S.; Yu, J. general approach to the synthesis of transition metal phosphide nanoarrays on MXene nanosheets for pH-universal hydrogen evolution and alkaline overall water splitting. *J. Mater. Chem. A* **2020**, *8*, 14234–14242. [CrossRef]
132. Wang, Z.; Yu, K.; Feng, Y.; Qi, R.; Ren, J.; Zhu, Z. Stabilizing $Ti_3C_2T_x$ -MXenes with $TiOF_2$ nanospheres intercalation to improve hydrogen evolution reaction and humidity-sensing performance. , *Appl. Surf. Sci.* **2019**, *496*, 143729. [CrossRef]
133. Zong, H.; Qi, R.; Yu, K.; Zhu, Z. Ultrathin Ti_2NT_x MXene-wrapped MOF-derived CoP frameworks towards hydrogen evolution and water oxidation. *Electrochim. Acta* **2021**, *393*, 139068. [CrossRef]
134. Yuan, Z.; Wang, L.; Cao, J.; Zhao, L.; Han, W. Ultraviolet-Assisted Construction of Nitrogen-Rich Ag@$Ti_3C_2T_x$ MXene for Highly Efficient Hydrogen Evolution Electrocatalysis and Supercapacitor. *Adv. Mater. Interfaces* **2020**, *7*, 2001449. [CrossRef]
135. Wang, X.; Wang, S.; Qin, J.; Xie, X.; Yang, R.; Cao, M. Constructing Conductive Bridge Arrays between $Ti_3C_2T_x$ MXene Nanosheets for High-Performance Lithium-Ion Batteries and Highly Efficient Hydrogen Evolution. *Inorg. Chem.* **2019**, *58*, 16524–16536. [CrossRef] [PubMed]
136. Dezheng, G.; Xin, L.; Yanqing, J.; Haijing, Y.; Aiping, W.; Ganceng, Y.; Yu, W.; Chungui, T.; Honggang, F. A dual-active Co-CoO heterojunction coupled with Ti_3C_2-MXene for highly-performance overall water splitting. *Nano Res.* **2021**, *15*, 238–247.
137. Attanayake, N.H.; Abeyweera, S.C.; Thenuwara, A.C.; Anasori, B.; Gogotsi, Y.; Sun, Y.; Strongin, D.R. Vertically Aligned MoS_2 on Ti_3C_2 (MXene) as an Improved HER Catalyst. *J. Mater. Chem. A* **2018**, *6*, 16882–16889. [CrossRef]
138. Li, X.; Lv, X.; Sun, X.; Yang, C.; Zheng, Y.Z.; Yang, L.; Li, S.; Tao, X. Edge-oriented, high-percentage 1T′-phase MoS_2 nanosheets stabilize Ti_3C_2 MXene for efficient electrocatalytic hydrogen evolution. *Appl. Catal. B* **2021**, *284*, 119708. [CrossRef]
139. Shinde, P.V.; Mane, P.; Chakraborty, B.; Sekhar Rout, C. Spinel $NiFe_2O_4$ nanoparticles decorated 2D Ti_3C_2 MXene sheets for efficient water splitting: Experiments and theories. *J. Colloid Interface Sci.* **2021**, *602*, 232–241. [CrossRef]
140. Kuang, P.; He, M.; Zhu, B.; Yu, J.; Fan, K.; Jaroniec, M. 0D/2D NiS_2/V-MXene composite for electrocatalytic H_2 evolution. *J. Catal.* **2019**, *375*, 8–20. [CrossRef]
141. Liang, J.; Ding, C.; Liu, J.; Chen, T.; Peng, W.; Li, Y.; Zhang, F.; Fan, X. Heterostructure engineering of Co-doped MoS_2 coupled with Mo_2CT_x MXene for enhanced hydrogen evolution in alkaline media. *Nanoscale* **2019**, *1*, 10992–11000. [CrossRef]
142. Li, S.; Que, X.; Chen, X.; Lin, T.; Sheng, L.; Peng, J.; Li, J.; Zhai, M. One-Step Synthesis of Modified Ti_3C_2 MXene-Supported Amorphous Molybdenum Sulfide Electrocatalysts by a Facile Gamma Radiation Strategy for Efficient Hydrogen Evolution Reaction. *ACS Appl. Energy Mater.* **2020**, *3*, 10882–10891. [CrossRef]
143. Yu, C.; Cao, Z.F.; Yang, F.; Wang, S.; Zhong, H. MoS2 confined on graphene by triethanolamine for enhancing electrocatalytic hydrogen evolution performance. *Int. J. Hydrogen Energy* **2019**, *44*, 28151–28162. [CrossRef]
144. Yan, H.; Tian, C.; Wang, L.; Wu, A.; Meng, M.; Zhao, L.; Fu, H. Phosphorus-modified tungsten nitride/reduced graphene oxide as a high-performance, non-noble-metal electrocatalyst for the hydrogen evolution reaction. *Angew. Chem.* **2015**, *127*, 6423–6427. [CrossRef]
145. Jiao, M.; Chen, Z.; Zhang, X.; Mou, K.; Liu, L. Multicomponent N doped graphene coating Co@Zn heterostructures electrocatalysts as high efficiency HER electrocatalyst in alkaline electrolyte. *Int. J. Hydrogen Energy* **2020**, *45*, 16326–16336. [CrossRef]
146. Li, B.; Li, Z.; Pang, Q.; Zhang, J.Z. Core/shell cable-like Ni3S2 nanowires/N-doped graphene-like carbon layers as composite electrocatalyst for overall electrocatalytic water splitting. *Chem. Eng. J.* **2020**, *401*, 126045. [CrossRef]
147. Lei, Z.; Xu, S.; Wu, P. Ultra-thin and porous MoSe2 nanosheets: Facile preparation and enhanced electrocatalytic activity towards the hydrogen evolution reaction. *Phys. Chem. Chem. Phys.* **2016**, *18*, 70–74. [CrossRef]

148. Yan, Y.; Xu, S.; Li, H.; Selvam, N.C.S.; Lee, J.Y.; Lee, H.; Yoo, P.J. Perpendicularly anchored ReSe2 nanoflakes on reduced graphene oxide support for highly efficient hydrogen evolution reactions. *Chem. Eng. J.* **2021**, *405*, 126728. [CrossRef]
149. Zhu, M.; Yan, Y.; Yan, Q.; Yin, J.; Cheng, K.; Ye, K.; Zhu, K.; Yan, J.; Cao, D.; Wang, G. In situ growth of Ni0· 85Se on graphene as a robust electrocatalyst for hydrogen evolution reaction. *Int. J. Hydrogen Energy* **2020**, *45*, 10486–10493. [CrossRef]
150. Bolar, S.; Shit, S.; Samanta, P.; Murmu, N.C.; Kolya, H.; Kang, C.-W.; Kuila, T. Conducting scaffold supported defect rich 3D rGO-CNT/MoS_2 nanostructure for efficient HER electrocatalyst at variable pH. *Compos. Part B Eng.* **2022**, *230*, 109489. [CrossRef]
151. Nguyen, V.-T.; Ha, H.; Nguyen, N.-A.; An, H.; Kim, H.Y.; Choi, H.-S. In situ engineering of Pd nanosponge armored with graphene dots using Br-toward high-performance and stable electrocatalyst for the hydrogen evolution reaction. *ACS Appl. Mater. Interfaces* **2020**, *12*, 15500–15506. [CrossRef] [PubMed]
152. Li, J.-S.; Li, J.-Y.; Huang, M.-J.; Kong, L.-X.; Wu, Z. Anchoring RuxP on 3D hollow graphene nanospheres as efficient and pH-universal electrocatalysts for the hydrogen evolution reaction. *Carbon* **2020**, *161*, 44–50. [CrossRef]
153. Li, Y.; Luo, Y.; Zhang, Z.; Yu, Q.; Li, C.; Zhang, Q.; Zheng, Z.; Liu, H.; Liu, B.; Dou, S. Implanting Ru nanoclusters into N-doped graphene for efficient alkaline hydrogen evolution. *Carbon* **2021**, *183*, 362–367. [CrossRef]
154. Jiang, B.; Liang, K.; Yang, Z.; Guo, K.; Shaik, F.; Zheng, J. FeCoNiB@ Boron-doped vertically aligned graphene arrays: A self-supported electrocatalyst for overall water splitting in a wide pH range. *Electrochim. Acta* **2021**, *386*, 138459. [CrossRef]
155. Tian, Y.; Wei, Z.; Wang, X.; Peng, S.; Zhang, X.; Liu, W.-m. Plasma-etched, S-doped graphene for effective hydrogen evolution reaction. *Int. J. Hydrogen Energy* **2017**, *42*, 4184–4192. [CrossRef]
156. Zang, X.; Qin, Y.; Wang, T.; Li, F.; Shao, Q.; Cao, N. 1T/2H mixed phase MoS_2 nanosheets integrated by a 3D nitrogen-doped graphene derivative for enhanced electrocatalytic hydrogen evolution. *ACS Appl. Mater. Interfaces* **2020**, *12*, 55884–55893. [CrossRef]
157. Yu, C.; Shi, Y.; Yan, F.; Zhao, Y.; Zhu, C.; Zhang, X.; Zhang, X.; Chen, Y. Three-dimensional FeP nanotube arrays fabricated through electrostatic-repulsion-limited-nucleation strategy for high-efficiency hydrogen evolution. *Chem. Eng. J.* **2021**, *423*, 130240. [CrossRef]
158. Li, S.; Jian, X.; Liu, J.; Guo, S.; Zhou, C.; Zhang, P.; Yang, Y.; Chen, L. Phosphorus-doped Fe_3O_4 nanoflowers grown on 3D porous graphene for robust pH-Universal hydrogen evolution reaction. *Int. J. Hydrogen Energy* **2020**, *45*, 4435–4443. [CrossRef]
159. Sun, Y.; Xu, K.; Zhao, Z.; Li, X.; Chen, G.; Li, C. Strongly coupled dual zerovalent nonmetal doped nickel phosphide nanoparticles/N, B-graphene hybrid for pH-Universal hydrogen evolution catalysis. *Appl. Catal. B Environ.* **2020**, *278*, 119284. [CrossRef]
160. Chen, C.; Luo, W.; Li, H.; Hu, T.; Zhao, Y.; Zhao, Z.; Sun, X.; Zai, H.; Qi, Y.; Wu, M. Optimized MoP with Pseudo-Single-Atom Tungsten for Efficient Hydrogen Electrocatalysis. *Chem. Mater.* **2021**, *33*, 3639–3649. [CrossRef]
161. Li, G.; Wang, J.; Yu, J.; Liu, H.; Cao, Q.; Du, J.; Zhao, L.; Jia, J.; Liu, H.; Zhou, W. Ni-Ni_3P nanoparticles embedded into N, P-doped carbon on 3D graphene frameworks via in situ phosphatization of saccharomycetes with multifunctional electrodes for electrocatalytic hydrogen production and anodic degradation. *Appl. Catal. B Environ.* **2020**, *261*, 118147. [CrossRef]
162. Karaman, C.; Karaman, O.; Atar, N.; Yola, M.L. Tailoring of cobalt phosphide anchored nitrogen and sulfur co-doped three-dimensional graphene hybrid: Boosted electrocatalytic performance towards hydrogen evolution reaction. *Electrochim. Acta* **2021**, *380*, 138262. [CrossRef]
163. Han, A.; Zhou, X.; Wang, X.; Liu, S.; Xiong, Q.; Zhang, Q.; Gu, L.; Zhuang, Z.; Zhang, W.; Li, F.; et al. One-step synthesis of single-site vanadium substitution in 1T-WS_2 monolayers for enhanced hydrogen evolution catalysis. *Nat. Commun.* **2021**, *12*, 709. [CrossRef]
164. Chen, Z.; Liu, X.; Xin, P.; Wang, H.; Wu, Y.; Gao, C.; He, Q.; Jiang, Y.; Hu, Z.; Huang, S. Interface engineering of NiS@MoS_2 core-shell microspheres as an efficient catalyst for hydrogen evolution reaction in both acidic and alkaline medium. *J. Alloy. Compd.* **2021**, *853*, 157352. [CrossRef]
165. Kumar, S.; Sahoo, P.K.; Satpati, A.K. Electrochemical and SECM investigation of MoS_2/GO and MoS_2/rGO nanocomposite materials for HER electrocatalysis. *ACS Omega* **2017**, *2*, 7532–7545. [CrossRef]
166. Wang, Z.; Xu, W.; Yu, K.; Fenga, Y.; Zhu, Z. 2D heterogeneous vanadium compound interfacial modulation enhanced synergistic catalytic hydrogen evolution for full pH range seawater splitting. *Nanoscale* **2020**, *12*, 6176–6187. [CrossRef]
167. Ye, W.; Fang, X.; Chen, X.; Yan, D. A three-dimensional nickel-chromium layered double hydroxide micro/nanosheet array as an efficient and stable bifunctional electrocatalyst for overall water splitting. *Nanoscale* **2018**, *10*, 19484–19491. [CrossRef]
168. Li, K.; Guo, D.; Kang, J.; Wei, B.; Zhang, X.; Chen, Y. Hierarchical hollow spheres assembled with ultrathin CoMn double hydroxide nanosheets as trifunctional electrocatalyst for overall water splitting and Zn air battery. *ACS Sustain. Chem. Eng.* **2018**, *6*, 14641–14651. [CrossRef]
169. Liu, S.; Zhu, J.; Sun, M.; Ma, Z.; Hu, K.; Tomohiko, N.; Liu, X.; Schmuki Patrik, S.; Wang, L. Promoting the hydrogen evolution reaction through oxygen vacancies and phase transformation engineering on layered double hydroxide nanosheets. *J. Mater. Chem. A* **2020**, *8*, 2490–2497. [CrossRef]
170. Li, Y.; Zhu, S.; Xu, Y.; Ge, R.; Qu, J.; Zhu, M.; Li, W. FeS_2 bridging function to enhance charge transfer between MoS_2 and g-C_3N_4 for efficient hydrogen evolution reaction. *Chem. Eng. J.* **2020**, *521*, 127804. [CrossRef]